PALEOCENE DEPOSITIONAL HISTORY OF THE CRETACEOUS-PALEOGENE IMPACT BASIN, YUCATAN PENINSULA, MEXICO

By

Katherine E. O'Malley

A Thesis Submitted in Partial Fulfillment of the Requirements

for the Degree of

MASTER OF SCIENCE

in

Geoscience

University of Alaska Fairbanks

December 2020

APPROVED:

Dr. Michael Whalen, Committee Chair
Dr. Sarah Fowell, Committee Member
Dr. Paul McCarthy, Committee Member
Dr. Paul McCarthy, Chair
Department of Geosciences
Dr. Kinchel Doerner, Dean
College of Natural Science and Mathematics
Dr. Richard Collins
Director of the Graduate School

Abstract

In the spring of 2016, the International Ocean Discovery Program set out on Expedition 364 to recover core from the peak ring of Chicxulub Impact Crater at Site M0077. In total, 829 m of core was collected spanning granite to Paleogene sedimentary rocks. From this core, we have a well-preserved record of the Paleocene, which represents ~10 million years post impact in just under 10 m of sedimentary rock record. This has presented an incredible research opportunity, as we have gained invaluable information on how the environment responded and recovered from the global catastrophe that was the Chicxulub Impact.

The Paleocene at M0077 is highly condensed and comprised of predominantly pelagic carbonate rocks. High resolution core logging and thin section analysis were used to identify facies in the Paleocene. Facies include marlstone, argillaceous wackestone, foraminiferal wackestone, and rare coarser grained lithologies such as packstone and grainstone. Overall, the Paleocene exhibits a succession of rhythmically bedded cycles composed of marlstones grading to argillaceous wackestones and capped by foraminiferal wackestones. Coarser grained lithologies only exist in the lower and uppermost portion of the core. In total, 72 cycles that ranged from 5-30 cm thick are identified and grouped into six larger packages based on pattern similarities in color, lithology, ichnofabric indices, and geochemical data. These cycles are interpreted as parasequences, and show predictable stacking patterns that allow us to make sequence stratigraphic analyses. Each package represents one to two systems tracts, and some can be correlated to eustatic sea level change. Recorded in this core is the progression of an initial sea level lowstand immediately post impact, and the fluctuation between highstands, lowstands, and transgressive systems tracts that follow.

Major and trace elements were analyzed throughout the core, as well as $\delta^{13}C_{org}$ and $\delta^{15}N_{bulk}$ values. Three sets of geochemical proxies (paleoredox, detrital input, productivity) were used to provide insight into paleoecological conditions. Initial conditions in the crater show a period of high productivity, which tapers off within a million years post impact. Redox conditions vary, and show one major anoxic event, with other enrichments likely representing periods of pore water euxinia or increases in stratification leading to a more robust redox gradient.

Table of Contents

List of Figures

Page

Acknowledgements

This project was supported by the University of Alaska Fairbanks Department of Geosciences. Funding was provided through National Science Foundation grant OCE 1737199 (to M.Whalen) and the Barringer Family Fund for Meteorite Impact Research (2017). This project was made possible by IODP Expedition 364, and the University of Bremen for access to the core repository. Special thanks to my advisor Dr. Michael Whalen, who provided guidance, knowledge, and numerous edits; my committee members Drs. Sarah Fowell and Paul McCarthy for edits and advice; Ken Severin and Nathan Graham for all the help with the XRF and its routines; Bryan Bosserman for helping me with sample preparation; April Knox and Deirdre LaBounty for all the advice; and Dustin Stewart, Veselina Yakimova, Jamshid Moshrefzadeh, Mark McClernan, Alby Harris, Trevor Waldien and Colby Paul for all the support and friendship. Lastly, endless thanks to my husband, Mason Garland for supporting me and moving all the way to Alaska with me so I could pursue my goals.

Chapter 1

1. Introduction

The Chicxulub impact crater is the only known terrestrial impact structure to be directly linked to a mass extinction event (Schulte et al. 2010). At the end of the Cretaceous, a massive impactor collided with the earth causing the extinction of 75% of all species, most notably including non-avian dinosaurs (Alvarez et al., 1980, Jablonski et al., 1995). Immediately following the impact, large magnitude (>10) earthquakes caused large scale gravity flows and the collapse of local portions of the Yucatan Platform (Kring et al., 2007). Tsunamis generated from both the impact itself and related tectonic events reverberated throughout the Gulf, and evidence exists for local fires ignited by fallout from ejecta (Gulick et al., 2017). However, the effects of the impact did not end there. The primary compositions of the target rocks were carbonates and evaporites, a majority of the latter vaporized upon impact. An estimated 325 Gt of sulfur and 425 Gt of CO_2 were released upon impact (Artemeava et al., 2017). This ejection of sulfur caused an initial brief global cooling that lasted from several months up to a decade before sulfate aerosols were removed from the atmosphere (Vellekoop et al., 2017). Following this, a period of post impact warming occurred, caused by the ejected CO_2, which, having a longer residence time than sulfur, was able to cause climactic effects on a timescale on the order of hundreds to thousands of years (Pope et al., 1994; MacLeod et al., 2018).

How life recovered after the impact has been a topic of great interest, and has birthed several, sometimes conflicting hypotheses on the long-term effects in the oceans. Initial studies suggested a collapse of the vertical ^{13}C gradient, which was believed to be caused by a major reduction in surface water productivity (Hsu et al., 1985, Zachos et al., 1989). A drop in surface productivity allows ^{12}C to build up, thereby reducing the $\delta^{13}C$ in the surface waters. This

reduction brings surface $\delta^{13}C$ values down to those more often seen in deep waters. However, later work revealed that the benthic foraminifera accumulation rate (BFAR) varied across the globe (Alegret et al., 2012). Several sites in the Pacific reveal an increase in BFAR, where the Atlantic saw stability or decreases (Alegret et al., 2012). This challenges the notion that surface water productivity was drastically reduced, as benthic foraminifera rely on the export of organic matter to the seafloor. A new view emerged, that changes in export productivity varied spatially, and were controlled by ecological factors (Esmerey-Senlet et al., 2015) such as competitive exclusion by opportunists, species incumbency, and trophic interactions (Lowery et al., 2018). However, other work also suggests the role of chance in spatial distribution of recovery timing rather than ecological factors when recovery heterogeneity cannot be explained by other means. (Hull et al., 2011). This combination of ecological factors and random chance is supported by the re-emergence of a productive ecosystem in the crater itself less than 30 kyrs post impact (Lowery et al., 2018).

Recent work on redox conditions has returned more straightforward results. Data show that the return to pre-impact redox conditions varied across the globe. Some sites took less than 500 years (De Oca, 2013), while others suffered millennial-scale hypoxia and benthic community disruption on continental shelves (Vellekoop, 2014). This study sheds light on the redox and productivity conditions in the crater post impact and presents the results of new, high resolution core logging. Herein I examine the stratigraphic and ichnologic changes alongside major and trace elements and $\delta^{13}C_{org}$ and $\delta^{15}N_{bulk}$ stable isotopes to reconstruct and document the ecosystem recovery in the 10 million years post impact. The results from this study suggest a million-year long period of high productivity immediately following the impact, with

productivity then declining, and the entirety of the Paleocene was punctuated by two hyperthermal events that can be correlated globally.

2. Geological Setting

The Chicxulub impact structure is located on the Northern Yucatan Peninsula of Mexico, with half of the crater onshore, and the other half offshore (Figure 1) (Hildebrand et al., 1991). Approximately 200 km in diameter, Chicxulub is the only preserved peak ring crater on Earth (Morgan et al., 2016). Peak ring craters are a type of complex crater that are defined by a ring of peaks that surround the center of the crater. A peak ring is caused by the formation of a transient cavity and initial central uplift upon impact, this central uplift was over-heightened and gravitationally unstable and subsequently collapsed to form the peak ring (Morgan et al., 2016). Peak ring and other complex craters can only be formed by large impactors (Morgan et al., 2016).

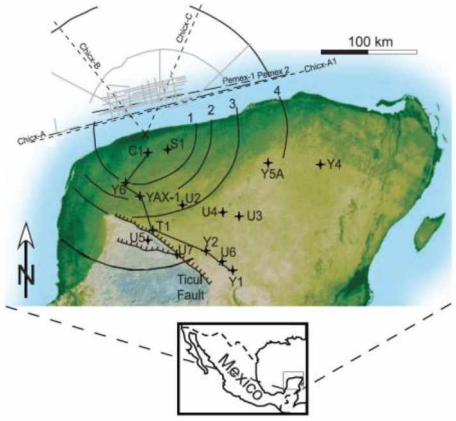

Figure 1 Crater Location on Mexico's Yucatan Peninsula, Whalen et al., 2013

The final crater morphology consists of a series of ring-shaped faults encircling the crater, inside the rim is a series of down-dropped blocks known as the "terrace zone" (Gulick et al., 2008). The terrace zone is a result of both the collapse of the central uplift, and down-dropping along fault planes (Collins et al., 2008). This zone dips beneath the annular trough and

peak ring. At the center of the crater lies a central basin, which overlies the buried central uplift and impact melt rocks (Figure 2) (Morgan et al., 2016)

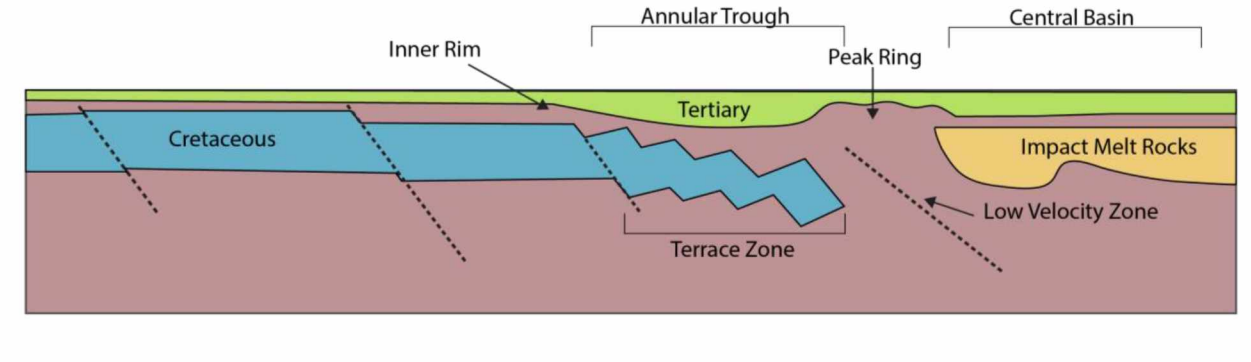

Figure 2 Cross Section of Chicxulub impact crater illustrating the morphology of the southern half of the crater, Modified from Morgan et al., 2016

Overall, Chicxulub has a distinct asymmetry with its northwestern and northeastern portions showing drastically different morphologies (Figure 3). Towards the northwest, the peak ring is more prominent, the faults are higher angle, and there are more faults that encompass a wider area (Gulick et al., 2008). However, towards the northeast, the peak ring is less prominent, the faults present are fewer and more listric (Gulick et al., 2008). In addition, unlike the northwest there is no inner rim present in the northeast (Gulick et al., 2008). These asymmetries in the crater are the result of pre-existing asymmetry. Prior to impact, the northwest had shallower waters, allowing more sediments to be ejected on impact and thus caused a more prominent peak ring due to a greater excavation depth allowing more basement uplift (Gulick et al., 2008). The opposite is true for the northeast, a region with deeper waters and less excavation (Gulick et al., 2008). These pre-existing asymmetries are the likely cause of the asymmetric crater morphology (Gulick et al, 2008).

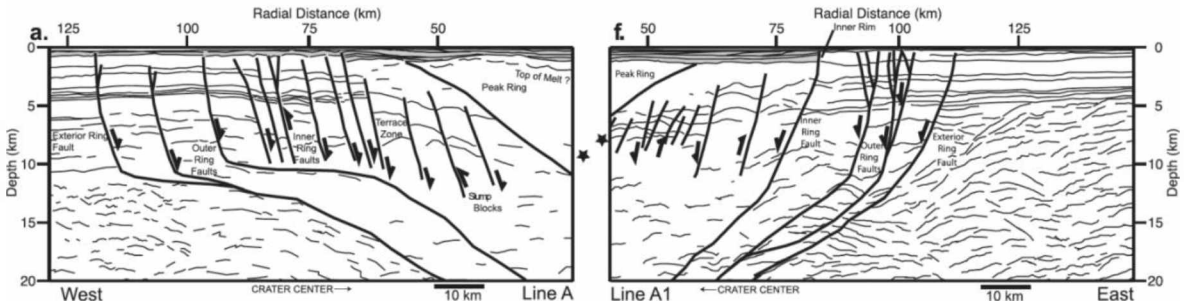

Figure 3 Crater Asymmetries along a EW cross section, Gulick et al., 2008

Prior to impact, during the end Cretaceous, climate was relatively stable until the Maastrichtian, when a Deccan-trap related warming period occurred (Li et al., 1999, Hollis et al., 2010). Sediments deposited on the Yucatan during this time were primarily composed of evaporites and carbonates, deposited in shallow water environments (Ward et al., 1995). The Cretaceous stratigraphy can be broken up into two general units: The Lower Cretaceous, which is primarily intertidal to shallow water evaporites with interbedded dolomite, and the Upper Cretaceous which is primarily shallow water carbonates and marls (Ward et al., 1995)

While most of the stratigraphic data prior to the mid-1990s came from Petroleos Mexicanos (PEMEX) boreholes, several more recent shallow cores drilled by the Universidad Nacional Autonoma de Mexico (UNAM) (Rebolledo-Vieyra et al., 2000) and the Yaxcopoil-1 (Yax -1) core from the Chicxulub Scientific Drilling Project (CDSP) (Urrutia-Fucugauchi et al., 2004) have further illuminated the structure and infill of the crater (Bell et al., 2004; Gulick et al., 2008; Whalen et al., 2013).

Overall, data from the Yax-1 core reveals a sedimentary succession of facies that represent slope and outer ramp platform environments (Whalen et al., 2013). Yax-1 sheds light on the sedimentary successions within the annular trough but because this location was on top of one of the terrace zone blocks, it contains abundant redeposited facies in the Paleocene portion of the core that complicate stratigraphic interpretations (Whalen et al. 2013). In the spring of 2016

the International Ocean Discovery Program (IODP) set out on Expedition 364 to drill into Chicxulub's peak ring (Site M0077) (Figure 4,5). This location was chosen not only to explore the peak ring itself, but because the Paleocene sediments are relatively undisturbed, allowing for a more complete look at the local recovery. Core was drilled from 505.7-1334.73 meters below seafloor (mbsf). The major units of the core include granitic basement, melt rock, breccia, a transitional unit, and post impact sedimentary rocks. 99% of the core was recovered, making the mission a major success. (Morgan et al., 2017)

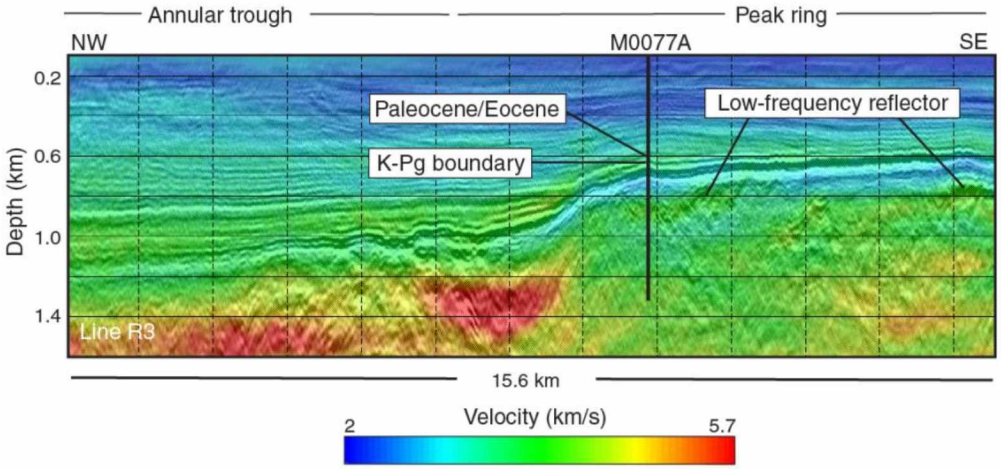

Figure 4 Position of IODP Core in Cross Section, Gulick et al., 2016

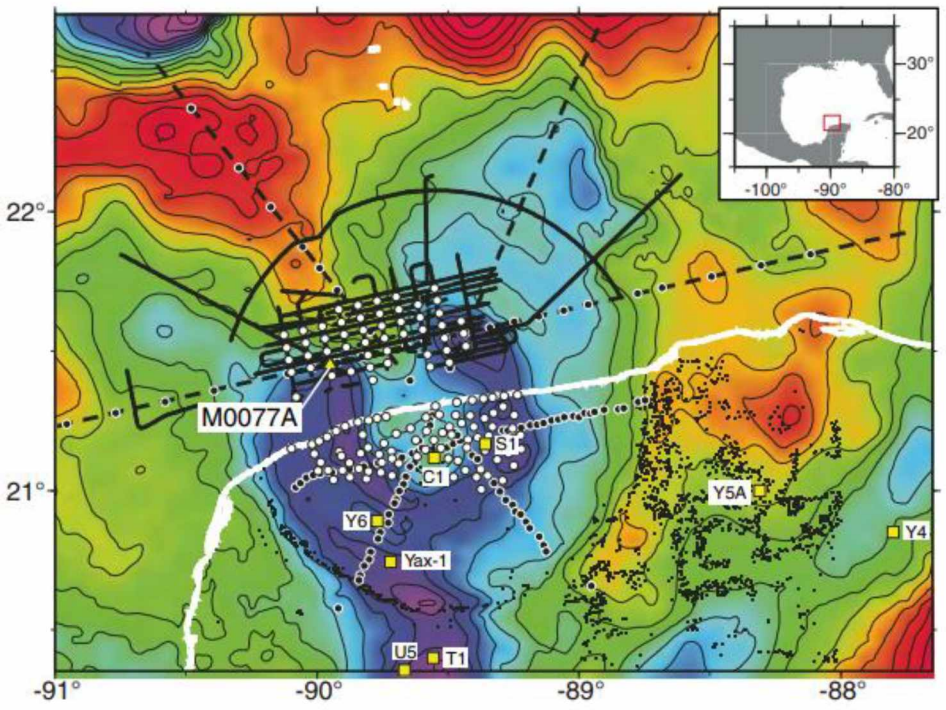

Figure 5 Location of Core with Gravity Data, Gulick et al., 2017

3. Methods

All samples were taken from site M0077, hole M0077A. Samples span most of the Paleocene, with the exception of the transitional unit. 50 samples were taken from 616.5 mbsf to 607.31 mbsf, spaced on average about 25 centimeters apart. 61 samples were taken to the Alaska Stable Isotope Facility for $\delta^{13}C_{org}$ and $\delta^{15}N_{bulk}$ analysis. This number exceeds the total sample number due to the fact that one particularly large (14cm) sample was subsampled and analyzed at the centimeter level yielding 14 additional samples. From the original 50 samples, thin sections were generated and were used for carbonate microfacies analysis, ichnofabric index (the degree of bioturbation, abbreviated as I.I.) and point counting.

3.1 Petrography

Traditional petrographic techniques were used to analyze 50 thin sections. These thin sections were described using carbonate microfacies analysis (Flugel, 2004) and depositional environments were interpreted. Rocks were classified based on Dunham (1962) as modified by Embry and Klovan (1972). Other observations documented include: carbonate grains and matrix, cement, clay content, sedimentary structures and textures, organic material, diagenetic alteration, and bioturbation. Bioturbation was given a numerical value as the ichnofabric index, which is the degree of sedimentary fabric disruption from bioturbation. This value ranges from 1 to 5 with 1 being undisturbed and 5 being homogenized (Droser and Bottjer, 1986,1989). Thin sections (n=18) were then selected at an interval of 0.5 m and point counted to a sampling target of 300 points to document small and large forams, lime mud, calcispheres, algae, brachiopods, gastropods, echinoderms, unknown bioclastic fragments, intraclasts, pyrite, and calcite cement.

3.2 Core Logging

The IODP 364 science party conducted initial core logging after drilling (Gulick et al., 2017). A more detailed log forms the sedimentological framework for this study. High resolution core logging was performed at the IODP Core Repository in Bremen, Germany. Documentation was made of every lithologic change and facies stacking patterns were identified. Detailed lithologic descriptions included color, contacts, sedimentary structures, ichnofabric index, visible fossils, secondary minerals, and other diagenetic features. The logged interval was 607.27 - 616.58 mbsf. Published color reflectance data (Gulick et al., 2017) was used for a quantitative analysis of lithologic color change. Color reflectance scan images were taken at the IODP core repository, and produced a high-resolution image output in the L*a*b system (Gulick et al., 2017). This provides a lightness variable (L*), which is a total reflectance value ranging

from 0 to 100. Clay content was visually estimated and then corroborated with the lightness variable. Intervals with a lower L* are inferred to have higher clay content, rare instances where lower L* values are attributed to TOC or disseminated pyrite in addition to higher clay content occur. Values around 50 L* are interpreted to have a high clay content, and increasingly higher L* values are interpreted to have decreasing clay content.

3.3 Age Estimation

Published biostratigraphic datums from M0077 (Lowery et al., 2018)(Figure 6) were used to estimate the age of the base of selected biostratigraphic zones. Each biozone was marked on our stratigraphic section at the published average depth, along with datum age. We then measured the stratigraphic thickness of each zone and counted the total number of stratigraphic cycles deposited within each zone. This number was then divided by the difference in age between the start and end of the biozone, and we were able to estimate the duration of each cycle.

Table 1, Biostratigraphic Datums from M0077, after Lowery et al., in review

Taxon	Zone	Sample Above	Sample Below	**Avg. Depth**	**Datum Age**
Discoaster multiradiatus	Base of CP8	607.26	607.37	**607.315**	**57.21**
Morozovella acuta	Base of P4b	607.52	607.76	**607.65**	**57.79**
*Heliolithus kleinpellii**	Base of CP5	607.52	607.76	**607.65**	**59.94**
Igorina pusilla	Base of P3a	609.28	609.3	**609.29**	**62.6**
Praemurica uncinata	Base of P2	610.6	610.65	**610.63**	**63**
Globanomalina compressa	Base of P1c	612.36	612.41	**612.385**	**63.9**
*Chiasmolithus danicus**	Base of CP2	612.5	612.75	**612.625**	**64.81**
Subbotina triloculinoides	Base of P1b	615.21	615.26	**615.235**	**65.25**
Parvularugoglobigerina eugubina	Base of P1a	616.15	616.2	**616.175**	**65.72**
Parvularugoglobigerina eugubina	Base Pα	616.56	616.56	**616.56**	**66**

3.4 X-Ray Fluorescence Spectroscopy

All geochemical work was conducted from our suite of samples, however due to sample size constraints only 42 samples could be analyzed for major and trace element studies. Major and trace elements are a valuable tool in marine sedimentology as they provide insight into a number of palaeoceanographic variables. In this study we use three sets of proxies: paleoredox (Mo, Cr), productivity (Ni, Cu, Zn, Ba), and detrital input (Si, Ti, Al) to establish the paleoenvironmental conditions within the crater in the years post-impact. These proxies were chosen on the following bases:

Molybdenum: Molybdenum (Mo) is the most common transition metal in the ocean, is most often present in the water column in the form of molybdate (MoO_4^{2-}), and has a long residence time of ~400kyr (Tribovillard et al., 2015). Mo is used primarily as a proxy for euxinia, as under sulfide-rich conditions molybdate readily converts to thiomolybdate ($MoO_{4-x}S_x^{2-}$) (Tribovillard et al., 2015). Under non-euxinic conditions, buried Mo often diffuses back into the water column, so there is little possibility of authigenic sediment enrichment. Under euxinic conditions however, thimolybdate is buried with organic matter and pyrite and is sequestered (Tribovillard et al., 2015). In conditions with an euxinic water column, Mo concentrations can exceed hundreds of ppm. In settings where euxinia is restricted to pore fluids, Mo concentrations can range from < 10 ppm to 25 ppm (Scott and Lyons 2012). In settings lacking euxinia in either the water column or pore fluid, concentrations stay around the average continental crust value of 1-2 ppm (Scott and Lyons, 2012). In addition, Mo and total organic carbon (TOC) have a strong covariation within euxinic settings (Algeo and Lyons, 2006). Within euxinic sediments, Mo/TOC ratios range from 25-30, whereas in Mo-depleted water columns and non-euxinic settings ratios are 10-15 and <2 respectively (Scott and Lyons 2012).

Chromium: Chromium (Cr) is used as a proxy for anoxia. It has a relatively short residence time of 7-40 kyr. In oxic conditions, chromium is most commonly present as Cr (VI) in the chromate anion $CrO_4^{2-}$and is soluble. However, in anoxic conditions, Cr reduces and forms aquahydroxyl and hydroxyl cations ($Cr(OH)_2^+$, $Cr(OH)_3$, $(Cr,Fe)(OH)_3$). These cations complex with humic and fulvic acids or adsorb to Fe- and Mn-oxyhydroxides. In this manner, Cr is buried within the sediment and causes enrichments (Tribovillard et al., 2015). Unlike Mo, Cr has a strong detrital influence and can also be buried with the land-derived clastic fraction (clay minerals, chromite, ferromagnesian minerals) due to its ability to readily substitute with Mg (Tribovillard et al., 2015). Consequently, small enrichments may be indistinguishable from this detrital component without isotopic analysis. Cr enrichments are compared against the crustal average of 11 ppm (Cole et al., 2017).

Nickel: Nickel (Ni) is used as a productivity proxy, as in oxic marine conditions it often acts as a micronutrient. In oxygenated environments, it is most commonly present as $NiCO_3$, which is soluble. In the water column, Ni will complex with organic matter (OM) which in turn accelerates scavenging and will ultimately enrich the sediment. Under reducing conditions, Ni can be released back into the water column, and under sulfate reducing conditions, Ni can be incorporated into pyrite as NiS. So, while being a valuable proxy for paleoproductivity, alteration from redox conditions needs to be taken into consideration (Tribovillard et al., 2006)

Copper: Copper (Cu) is used as a productivity proxy, as in oxic marine conditions it acts as a micronutrient. In oxygenated environments, it's most commonly present as organometallic ligands and $CuCl^+$ ions. Like Ni, Cu will complex with OM which in turn accelerates scavenging and sediment enrichment. Unlike Ni, under reducing conditions Cu is incorporated as a solid solution pyrite phase and not released into the water column (Tribovillard et al., 2015).

Barium: Barium (Ba) is used as a productivity proxy in oxic marine conditions. It is most commonly present in the form of barite ($BaSO_4$) within detrital plagioclase crystals. Phytoplankton incorporate Ba through adsorption or metabolic intake, and upon death and decay barite may precipitate. Due to this relationship between barite and OM, Ba is used as a proxy for paleoproductivity and can be specifically used for export productivity (Tribovillard et al., 2015). However, Ba deposited under oxic conditions may be subject to release under subsequent anoxic conditions, which can then reform as barite again under oxic conditions, so care must be applied in distinguishing this diagenetic barite from barite that is linked to productivity (Tribovillard et al., 2015).

Zinc: Zinc (Zn) is used as a productivity proxy as in oxic marine conditions it acts as a micronutrient (Tribovillard et al., 2015). It is most commonly present as complexes with humic/fluvic acids, but can be present as $ZnCl^+$ions or Zn^{2+} cations. Under reducing conditions it, like Cu, can be incorporated as a solid solution pyrite phase or form sphalerite ((Zn,Fe)S) (Tribovillard et al., 2015)

Silica, Titanium, and Aluminum: Silica (Si), Titanium (Ti), and Aluminum (Al) are all ubiquitous elements in clastic rocks and generally speaking are not found in authigenic minerals within a carbonate platform, therefore an increase in these elements represents an increase in detrital input from land derived clastic sources. In addition, Al and Ti are immobile elements. Due to this, they are especially useful as a normalization factor for trace element studies.

Samples were measured for elemental abundances using the University of Alaska Fairbanks Advanced Instrumentation Laboratory (UAF AIL) PANalytical Axios wavelength-dispersive X-Ray Fluorescence Spectrometer (XRF). Elemental routines were based on those of

Sliwinski et al. (2012), that were created to detect low concentrations (0-50 ppm) of trace elements. Analytes were calibrated against certified geologic standard reference materials and refined with proven samples and their published datasets (Sliwinski et al., 2012). Calibrations to the XRF were applied shortly before experiments, and the accuracy of the calibration relative to the standards is within 10%.

10 g of each sample was powdered using steel vials and pressed into 35 mm pellets with a polyvinyl alcohol (PVA) binder. Two of the samples had to be pressed into 27 mm pellets due to small sample size (~7 g). Upon completion of the XRF routine, all data was normalized to Al.

3.5 Isotopic Analysis

Samples (n=61) were used for whole rock analyses of $\delta^{13}C_{org}$ and $\delta^{15}N_{bulk}$ values. 1 g of each powdered sample was acidified with an excess of 1M HCL. Acid-insoluble residues were rinsed, freeze dried, then analyzed for C and N values using the Thermo Scientific Flash 2000 elemental analyzer and Thermo Scientific Conflo IV interfaced with a Thermo Scientific DeltaVPlus Mass Spectrometer. Stable isotope ratios were reported in δ notation as parts per thousand (‰) deviation from the international standards VPDB (carbon) and Atmospheric-Air (nitrogen). Typically, instrument precision is <0.2 ‰. Analyses were performed by the Alaska Stable Isotope Facility at the University of Alaska Fairbanks's Water & Environmental Research Center. Organic C in the acid insoluble portion was used to generate the whole rock TOC by calculating mass lost during acidification, which also yielded a total carbonate content. The analytical precision and accuracy associated with these analyses is within 2% for TOC and 10% for $CaCO_3$. Three of the 61 samples were improperly prepared, produced erroneous results, and were not used in this study.

4. Results

4.1 Stratigraphy

A combination of high-resolution core logging and petrographic analyses was used to document the stratigraphy of the Paleocene at Site M0077. This informed the macroscopic documentation while logging the entire section of core. With this combination of highly detailed core logging and petrography, five different lithologies were identified in the Paleocene at Site M0077:

Marl: Dark gray carbonate units that are thinly bedded to laminated and contain variable amounts of clay are referred to as marl. These units are usually less than 5 cm thick. Wispy solution seams are common, as are pyrite nodules and burrowing.

Claystone: Dark gray to light gray fine-grained, predominantly clay units that are thinly bedded and less consolidated than other lithologies are referred to as claystone. These units are usually less than 5 cm thick and appear as fragmented or broken beds due to their crumbly nature.

Argillaceous Wackestone: Medium to dark gray units that contain greater clay content than other wackestones from the core are referred to as argillaceous wackestone. Units are thinly bedded and locally laminated and are usually less than 10 cm thick. Macrofauna are sparse, but foraminifera are present throughout in low concentrations. Units are burrowed throughout, and wispy stylolites, stylolitic laminae, and pyrite nodules are common.

Foraminiferal Wackestone: Light gray units that contain greater foraminifera and lower clay content than argillaceous wackestones are referred to as foraminiferal wackestone. These units are bedded on the centimeter scale and are abundantly burrowed and bioturbated. These units

are usually less than 20 cm thick. Other bioclasts occur rarely, and are a minor component. Stylolites and stylolitic laminae are common throughout, and pyrite nodules occur locally.

Packstone: Medium to light gray to tan units that are grain-supported by lithoclasts and bioclast fragments that include foraminifera, brachiopods, algae and echinoderms are referred to as packstones. Units are thin to thickly bedded and are 5 to 30 cm thick. Large foraminifera are visible. Burrows and stylolitic laminae occur locally, and pyrite is rare in these units.

Grainstone: Light gray to tan units that are grain-supported and also lack lime mud are referred to as grainstones. Units are less than 10 cm thick. Grains in these units comprise bioclasts and lithoclasts. Lithoclasts are black, gray, and tan carbonate grains reaching up to very coarse sand size (1-2mm). Large foraminifera are visible, and other bioclast fragments occur but are unidentifiable. Burrowing is common, and large solution seams and stylolitic laminae occur locally.

4.2 Facies Associations and Lithologic Cycles

Overall, the core exhibits a rhythmic pattern throughout the section, containing cycles consisting of beds that typically grade from marl to argillaceous wackestone and are capped by a foraminiferal wackestone. In total there are 72 cycles that vary in thickness from 4.1 – 32.9 cm. Each of the 72 cycles begins with a darker and more clay-rich lithology as evidenced from changes in the *L values, and each cycle shows increases in carbonate and fossil content and ichnofabric index towards the top. Taking this data into account, each cycle represents a deepening event at its base and subsequent shallowing upward. While many cycles display

gradational contacts that are a result of bioturbation, clear changes in lithofacies color, grain size, and relict lamination permit subdivision of cycles. However, due to this bioturbation, cycle contacts may be imprecise at the scale of mm. Rarely, cycles are capped by coarser-grained lithologies (packstone, grainstone). Coarser-grained facies exist solely in the lower 20 cm and upper 1.5 m of the core. Other trends in the ichnofabric index, grain type and size, color reflectance data, and physical core color exhibit repeating patterns and distinct changes that permit us to divide the Paleocene into nine packages on the basis of these data and the stacking pattern of the lithologic cycles.

These packages share similar characteristics, each package typically begins with a very dark marl or argillaceous wackestone that has the lowest lightness variable (L*) within that package. Most packages show a color change, and typically go from medium/dark gray to light gray to white upwards in a stepwise manner. While each individual cycle exhibits a lightening upwards trend, together they show distinct patterns of color change that transcend the individual cycles. Lithologies with the highest L* are usually at the top of each package. Each cycle typically has a lower i.i. at its base that increases towards the top, a trend which is also observed in tandem with stepwise increases in lightness within the packages. The combination of distinct changes in lithology, stacking pattern, color reflectance, and i.i. values were the criteria used to select the boundaries between packages with each boundary showing a sharp contrast in these criteria between packages. Due to the distinct patterns seen in the small-scale cycles and large-scale packages, we interpret the 72 nested cycles as parasequences within larger-scale systems tracts that ultimately make depositional sequences. Parasequences are defined as a single shallowing upwards cycle bounded by flooding surfaces (Van Wagoner et al., 1988). Systems tracts are defined as stratigraphic units that represent different portions of a depositional

sequence that can be used to interpret changes in relative sea level (Van Wagoner et al., 1988). Depositional sequences are defined as sedimentary rocks that were deposited during, and record, one cycle of relative sea level change, including a fall and a rise. Depositional sequences and their systems tracts are identified by their facies stacking patterns and geometric relationship to adjacent units and stratal discontinutites that form their boundaries (Van Wagoner et al., 1988). Facies stacking patterns include retrogradational, aggradational, and progradational modes and were interpreted based on the following criteria:

Retrogradational: Facies stacking patterns and decreasing L* values indicate increasing clay content through each successive cycle and the entire package is interpreted as deepening upward. Each successive cycle was thus shifting landwards indicating that they are part of the transgressive systems tracts (TST)

Progradational: Facies stacking patterns and increasing L* values in each cycle upsection are interpreted to indicate shallowing upwards. Each successive cycle was shifting basinward as would occur in both highstand and lowstand systems tracts (HST, LST).

Aggradational: stacking patterns show no or minimal change in facies stacking patterns or L* values throughout the section, and are interpreted to indicate neither significant shallowing or deepening. Aggradational facies stacking patterns occur in both highstand and lowstand systems tracts. (Catuneanu et al., 2009)

Throughout the entire core, small foraminifera abundance shows an increasing trend upwards with a corresponding decrease in lime mud. Calcispheres show a decreasing trend from the base of the core upwards, and ultimately disappear within package two (Table A-1, appendix, Figure 7). Ichnotaxa seen throughout all packages are primarily *Zoophycos*, *Planolites*, and

Chondrites, with *Thallasinoides* and *Glossifungites* occurring only at the very top of the Paleocene. Further detail on each package will be discussed with the similarities outlined above in mind.

4.2.1 Sequence 1

Package 1, 616.58 – 616.04 mbsf

Package 1 is 0.54 m thick and comprised of 2 cycles. This first package contains the first carbonate sedimentary rocks above the "transitional unit" that records the transition between the underlying suevite and the normal marine sedimentary rocks above (Gulick et al., 2017). The lowermost 5 cm of package 1 is marl to argillaceous wackestone to packstone with an i.i. of 2. This most basal unit is green to medium dark gray with a relatively low lightness variable (L*) of ~45 (Figure 7) and contains one of the few coarse-grained facies in the entire Paleocene section. A thin section from 616.45 mbsf shows predominantly lime mud (78%) with calcispheres and small (<3 mm) foraminifera (Figure A-1, appendix). In stark contrast to the lowermost 5 cm, the first and second cycles are light gray to white, with a much higher L* of 6 at the base of the first. These light cycles are 26 and 31.6 cm thick, respectively, and contain little clay. Above the second light bed is a sharp contact with a much darker (59 L*) bed at 616.04 mbsf, marking the top of the package. The decrease in clay content and the thickening upward pattern are interpreted to record a progradational facies stacking pattern. The combination of coarser- grained facies, thick cycles, and high lightness variables support the interpretation that Package 1 is a lowstand systems tract (LST, L-1).

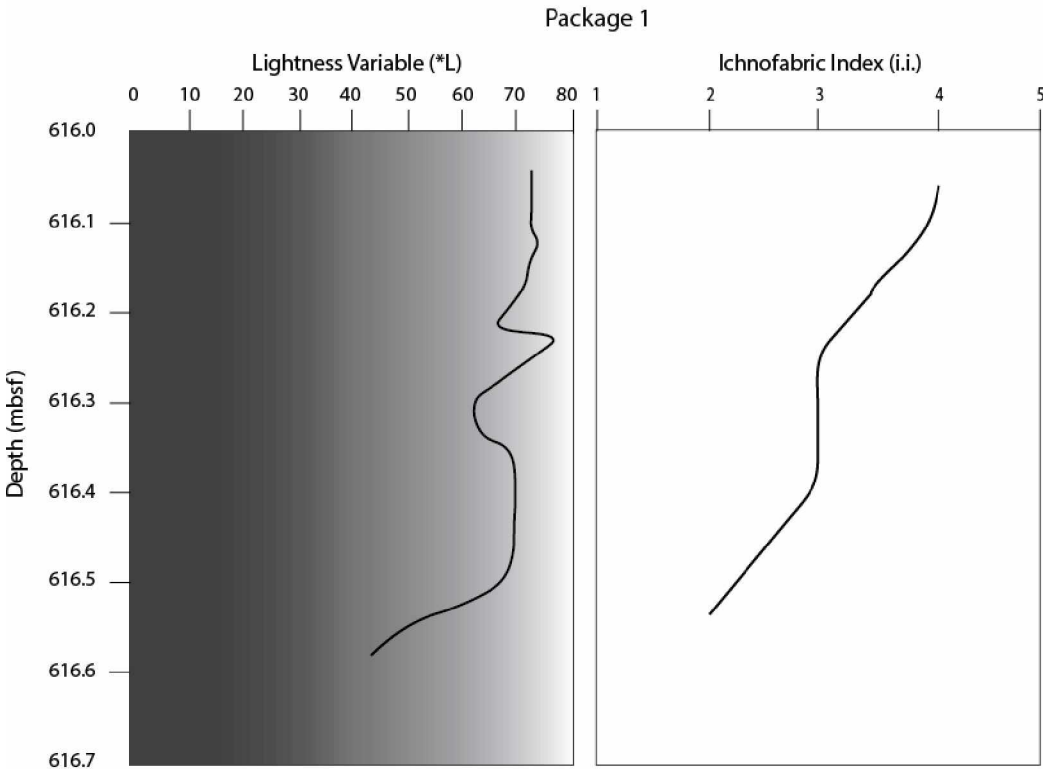

Figure 6, Package 1 Lightness Variable (L) and Ichnofabric Index vs Depth*

Package 2, 616.04 - 615.06 mbsf

Package 2 is 0.98 m thick and composed of 7 cycles. Thickness of these cycles varies from 6.7 cm to 32.9 cm. At its base is a dark wackestone with a color reflectance value of 56 L*(Figure 8). With the exception of the first dark cycle at 616.04 mbsf that is 6.7 cm thick, cycles until 615.28 mbsf show a thinning upwards trend, while the final two cycles thicken upward. At 615.71 mbsf the i.i. drops from 4 to 1. This is coincident with an increase in calcispheres (2%). After this, the i.i. resumes its overall increasing trend, and calcispheres disappear from the core completely (uppermost calcispheres located at 615.43 mbsf). The uppermost part of package 2 is a medium gray foraminiferal wackestone and has a color reflectance value of 61 L*.

Within package 2, there is a clear retrogradational stacking pattern. Cycles generally thin and increase in mud content towards the top. Coarser grained facies disappear and we begin to see the pattern of marl to argillaceous wackestone to foraminiferal wackestone in earnest. This is interpreted as a deepening upwards succession and a TST (T-1).

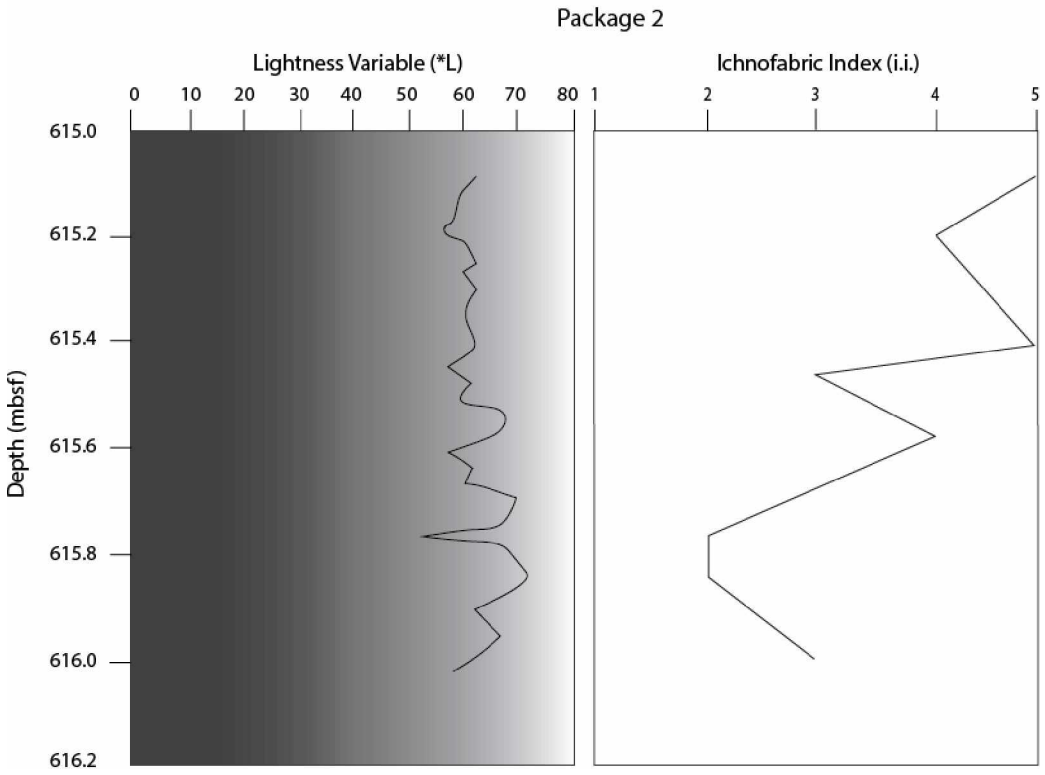

Figure 7, Package 2 Lightness Variable (L) and ichnofabric index vs Depth*

Package 3, 615.06 – 614.17 mbsf

Package 3 is 0.89 m thick and is composed of 7 cycles. Thickness of these cycles varies from 4.8 – 19.3 cm. The base is a dark gray argillaceous wackestone (51 L*) that displays a strong contrast with the underlying light to medium gray foraminiferal wackestone at the top of package 2 (Figure 9). The contact between these two packages is highly bioturbated (i.i. 3) and bioturbation progressively increases upward in a stepwise manner. The uppermost part of package 3 is a light gray foraminiferal wackestone and has a color reflectance value of 69 L*. At

its base, clay content is similar throughout each cycle, then begins to decrease at the very top of the package. This is interpreted to be an aggradational to progradational sequence, and supports an interpretation of a HST (H-1).

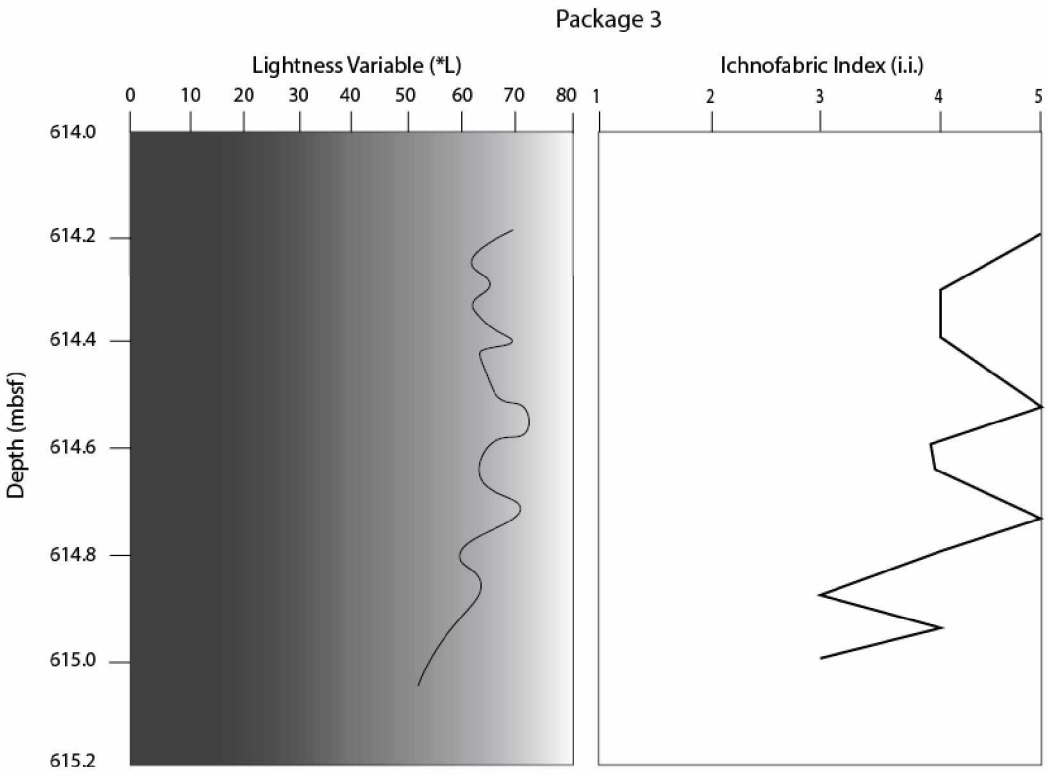

Figure 8, Package 3 Lightness Variable (L) and Ichnofabric Index vs Depth*

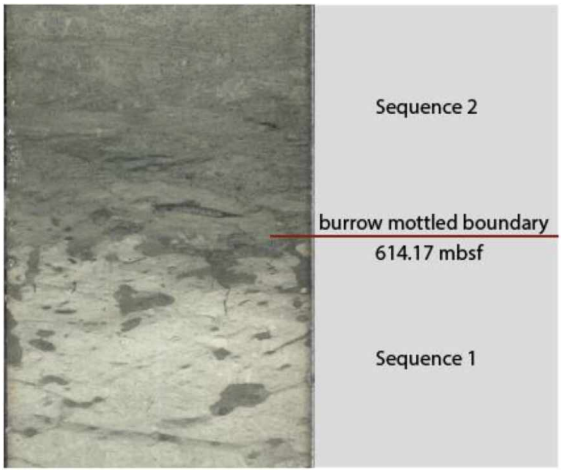

Figure 9, Bioturbated boundary between sequences

4.2.2 Sequence 2

Package 4, 614.17 – 613.03 mbsf

Package 4 is 1.14 m thick and consists of 9 cycles. Thickness of these cycles varies from 5.1 – 23.1 cm. The base of package 4 is completely bioturbated (i.i.=5, Figure 10) and a medium gray (55 L*) argillaceous wackestone (Figure 11). Within this package, point counting data shows little overall fluctuation, with only minor decreases in small foraminifera (43% to 35%) and cement content, while lime mud increases slightly from 44 to 47% (Figure A-1). Overall, clay content appears to increase upwards within this package. However, intense bioturbation clouds a qualitative estimate for the entire package. The uppermost part of package 4 is a medium gray foraminiferal wackestone and has a color reflectance value of 59 L*. Similar to the clay content, however, bioturbation obscures the precise upper boundary of the package.

Package 4's pattern of mud content increasing upsection through each cycle, paired with a darkening in color and decrease in grain size is interpreted to be a retrogradational stacking pattern, a deepening upwards, and a TST (T-2) of a second depositional sequence.

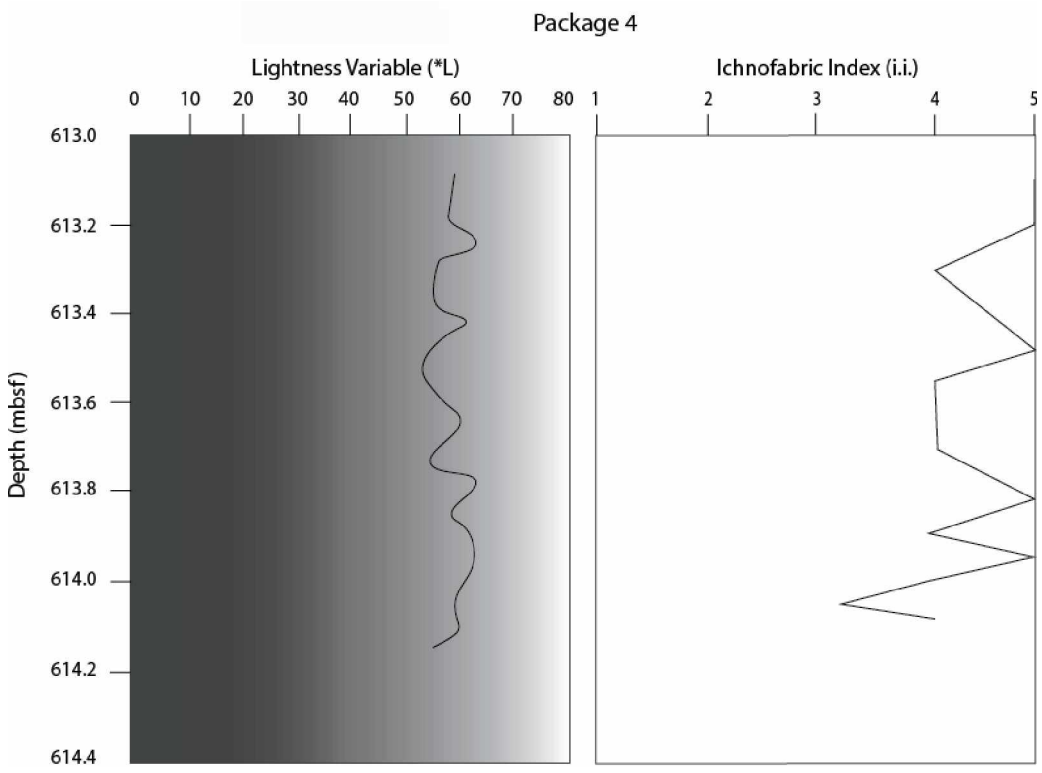

Figure 10, Package 4 Lightness Variable (L) and ichnofabric index vs Depth*

Package 5, 613.03 – 611.42 mbsf

Package 5 is 1.61 m thick and consists of 12 cycles. Thickness of these cycles varies from 6.5 -18.2 cm. The base of the package is a dark (51 *L) argillaceous wackestone (Figure 12). Clay content starts out high and progressively decreases to the top of the package. The uppermost part of package 5 is a light gray foraminiferal wackestone and has a color reflectance value of 62 L*. This lightening upwards trend is interpreted to be a HST (H-2).

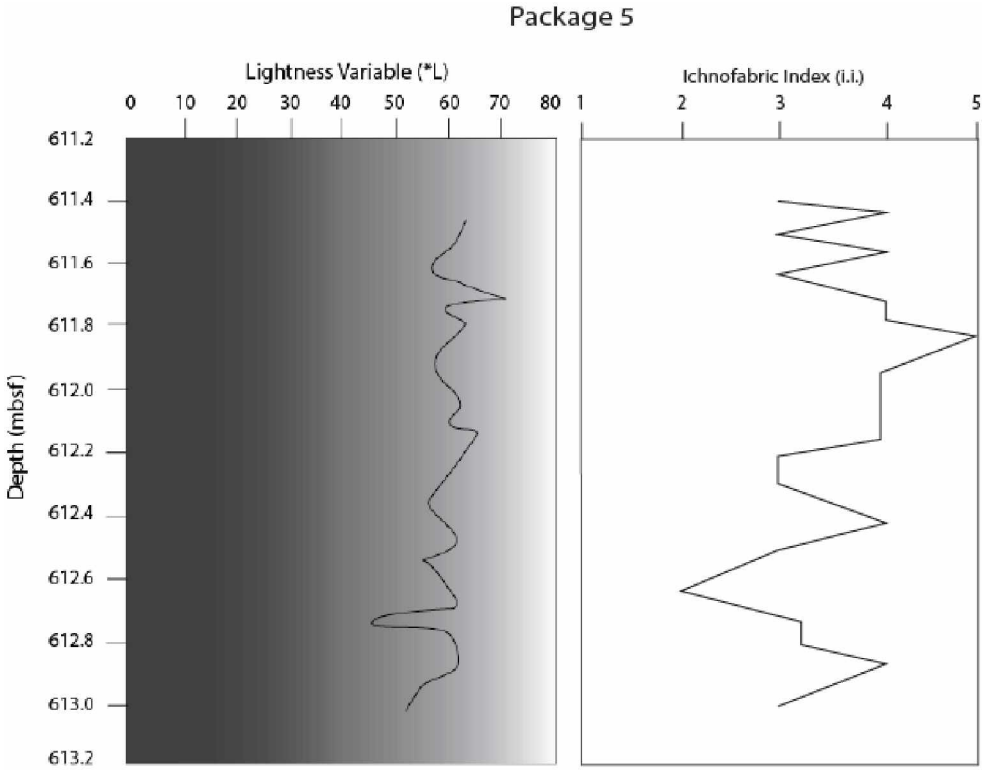

Figure 11, Package 5 Lightness Variable (L) and ichnofabric index vs Depth*

4.2.3 Sequence 3

Package 6, 611.42 – 609.64 mbsf

Package 6 is 1.78 m thick and consists of 13 cycles that begin with a medium gray (56 L*) argillaceous wackestone (Figure 13). Thickness of these cycles varies from 4.1 -22.9 cm. At its base, small foraminifera show a reduction (28%) from uppermost package 5 but increase throughout the package up to 45% (Figure A-1). Like the other packages, the i.i. varies from base to top within cycles, but shows no major changes overall. The uppermost part of package 6 is a medium gray foraminiferal wackestone and has a color reflectance value of 59 L*. Clay content increases upward within this package.

Package 6 exhibits an increase in argillaceous wackestone through each cycle upward, which at first glance appears to be a retrogradational stacking pattern. This increase in argillaceous wackestone, however, is coeval with an increase in Si, signaling an increase in detrital input suggesting this package is a LST. (L-2)

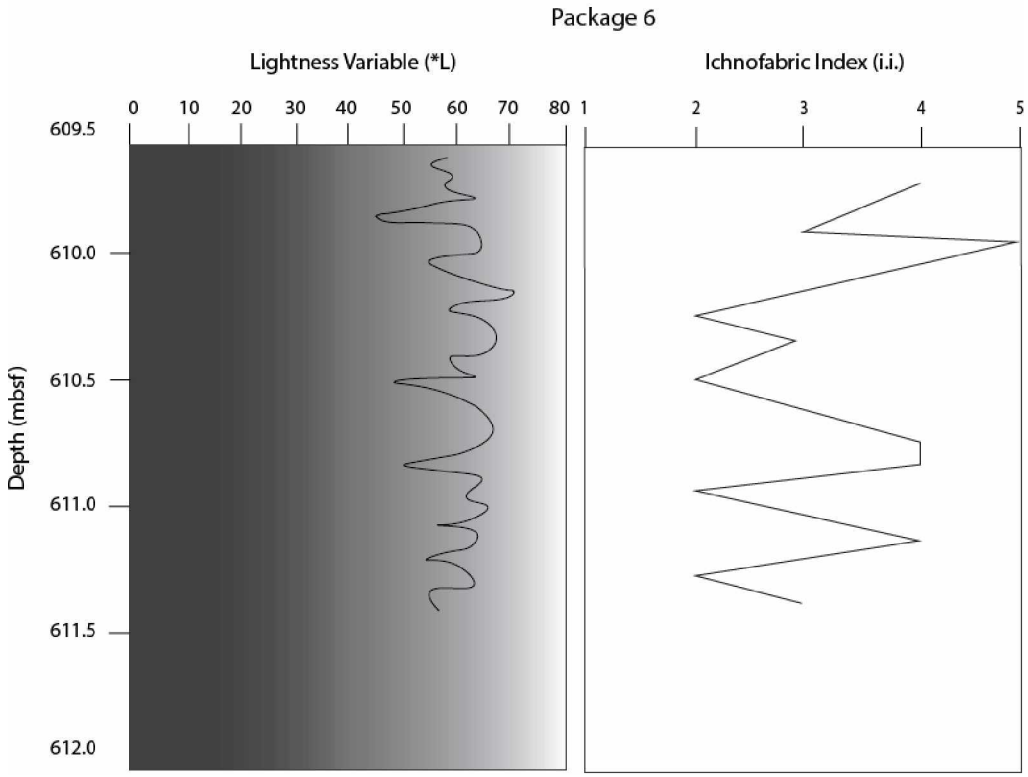

Figure 12, Package 6 Lightness Variable (L) and ichnofabric index vs Depth*

Package 7, 609.64 – 608.84 mbsf

Package 7 is 0.8 m thick and consists of 7 cycles. Thickness of these cycles varies from 7.1 – 14.7 cm. There is a slight thickening upwards trend of these cycles. The base of package 7 is a dark gray (47 L*) argillaceous wackestone (Figure 14). Small foraminifera reach a peak (45%, 609.59 mbsf) within this package (Figure A-1). Clay content decreases upsection.

Within this package, lime mud content decreases upsection, and each cycle exhibits a thickening upwards pattern. This is interpreted as a progradational stacking pattern. Package 7 is interpreted as a HST (H-3).

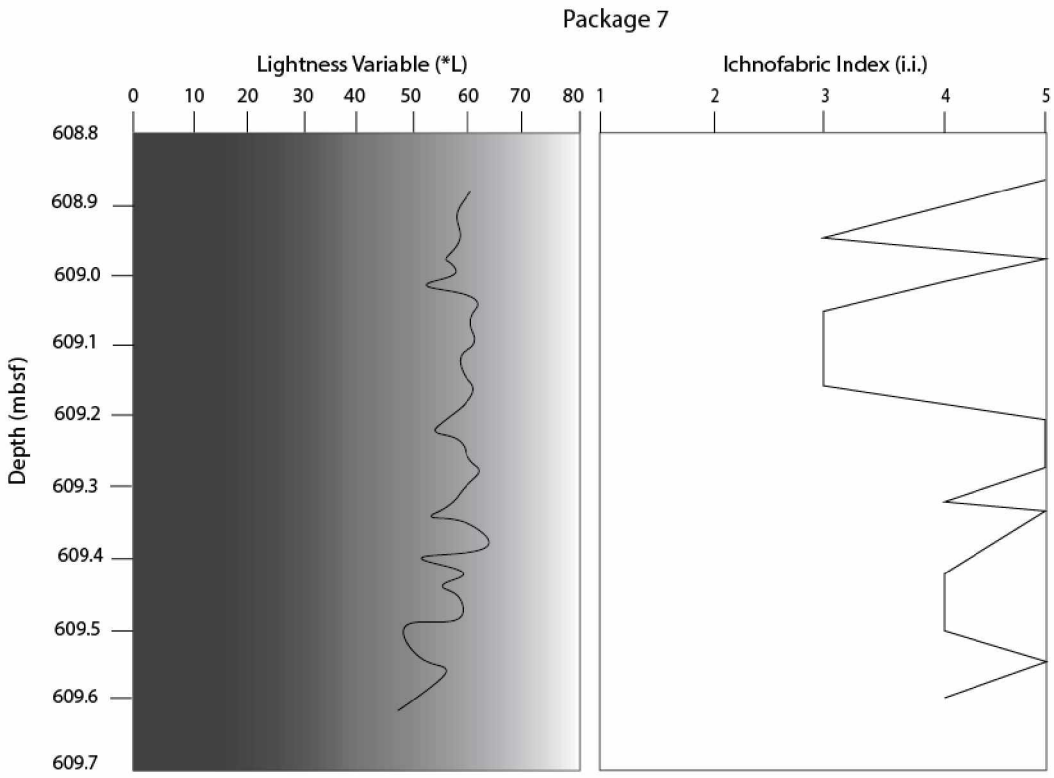

Figure 13, Package 7 Lightness Variable (L) and ichnofabric index vs Depth*

4.2.4 Sequence 4

Package 8, 608.84 – 607.74 mbsf

Package 8 is 1.1 m thick and consists of 13 cycles. Thickness of these cycles ranges from 5.5 – 17.8 cm, but cycles typically fall between 5 – 9 cm in thickness. The base of the package is a medium gray (57 L*) argillaceous wackestone that remains a consistent color throughout the section (58 L*, 607.74 mbsf) (Figure 15). Pyrite reaches a peak within this package (7.3%, 608.74 mbsf) (Figure A-1). Mud content varies within each cycle but appears to remain

consistent at the package scale. This is interpreted to be an aggradational facies stacking pattern and a LST (L-3). Package seven is capped by a claystone layer that's topped by an unconformity.

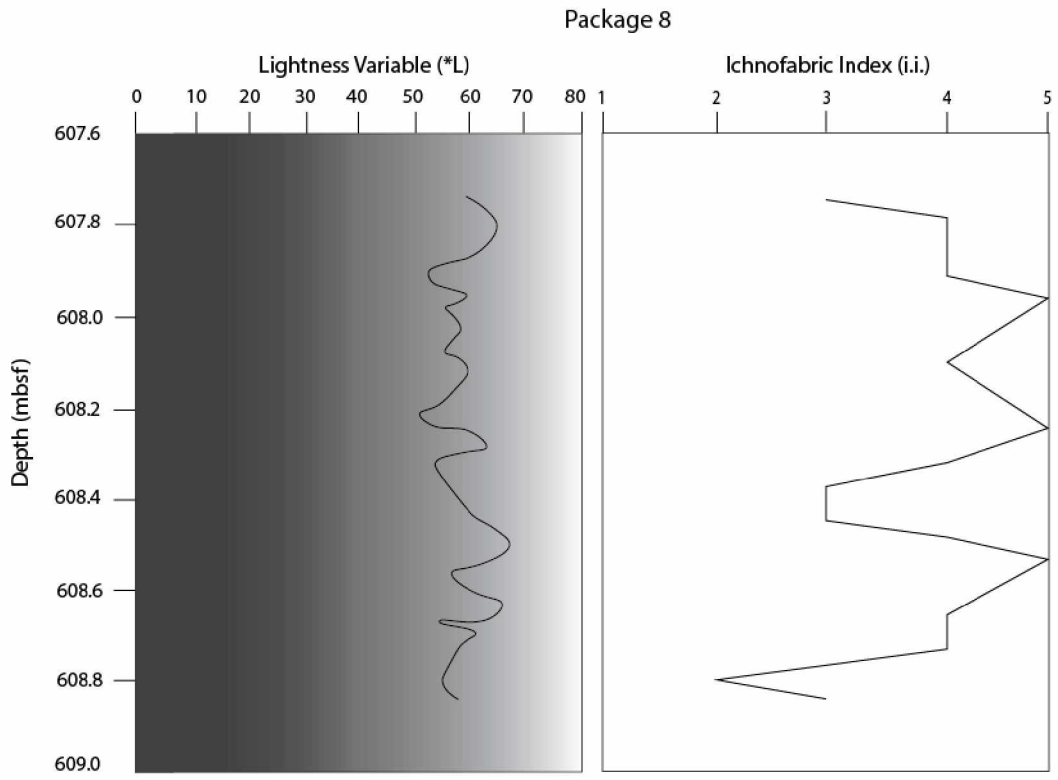

Figure 14, Package 8 Lightness Variable (L) and ichnofabric index vs Depth*

4.2.5 Sequence 5

Package 9, 607.74 – 607.27 mbsf

Package 9 is 47 cm thick and is the uppermost package of the Paleocene. This upper portion does not follow the general patterns documented in the packages below. At its base is a medium gray claystone layer that is 7.8 cm thick. This claystone underlies a 29.2 cm thick light gray to tan packstone that includes both bioclasts and lithoclasts and is highly bioturbated (i.i. 3-4)

(Figure A-1). Bioclasts include large foraminifera, algae, and echinoderm fragments. Separating the claystone and packstone is the first of two unconformities that punctuate the Upper Paleocene. Above the packstone is a 4 cm thick dark gray to black claystone layer that is topped by a 7.1 cm thick light gray to tan grainstone. This grainstone has abundant large lithoclasts and bioclasts that are up to pebble sized (largest 2cm). Lithoclasts include tan and gray intraclasts, and bioclasts include large foraminifera and fragmented echinoderms. The upper grainstone contains large burrows that are most likely *Thallasinoides*. The studied core is ultimately topped by a sharp contact with a laminated black shale, signaling the end of the Paleocene and the second unconformity seen (Smith et al., 2020). Package 9 is interpreted to be a LST (L-4) due to the erosional nature of its basal contact and input of shallow water biota.

4.3 X-Ray Fluorescence Spectroscopy

4.3.1 Redox proxies

Redox proxy results are summarized in Table A-2 (appendix) and Figure 16.

Chromium: The average Al-normalized value for Cr in the studied section was 5.7 ppm/wt%, and values range from 2.2 – 25.5 ppm/wt%. At the base of the section (616.08 mbsf) until 615.40 mbsf, there is a clear decreasing trend from 13.0 to 2.4 ppm/wt%. This is overlain by a small peak (614.64 mbsf, 5.8 ppm/wt%) then an interval of relatively stable values (614.3–611.41 mbsf, average 3.9 ppm/wt%). This stable interval is overlain by a sharp and drastic peak of 25.5 ppm/wt% at 611.14 mbsf. Following this is a decline until 610.17 mbsf, where values fall to 13.8 ppm/wt%. Cr values then decline (610.14 mbsf, 3.7 ppm/wt%), peak (609.02, 8.4 ppm/wt%), and decline again. From 608.74 mbsf to the top of the section (607.40 mbsf) values

hover around just below the average, and remain between 3.3 and 5.2 ppm/wt% with no major fluctuations.

Molybdenum: The average value of Al normalized Mo data in the studied section is 0.6 ppm/wt% and ranges from 0.03 – 2.8 ppm/wt%. Values start off at 0.8 then peak at 615.77 mbsf with a value of 1.8. Like Cr, this is followed by a decreasing trend until a small peak of 0.9 ppm/wt% at 614.64 mbsf. An area of little change follows (614.3 – 611.67 mbsf), which is overlain by a small peak (0.8 ppm/wt%, 611.41 mbsf). This slight peak occurs immediately prior to a large Cr peak. This is overlain by a decline to 0.03 ppm/wt% at 610.36 mbsf and a peak immediately following (0.7 ppm/wt% at 610.17 mbsf). Following this is a decline (0.3 ppm/wt%, 610.14 mbsf), a rebound (0.8 ppm/wt% at 609.02 mbsf) a decline again, and succeeded by the largest Mo peak of 2.8 ppm/wt% at 608.74 mbsf. From here to 608.07 mbsf, values return to near average, and do not fluctuate until 607.95 mbsf, where values increase again culminating in a peak of 2.2 ppm/wt% at 607.79 mbsf. A stepwise decrease is seen above, with a smaller peak of 1.1 ppm/wt% at 607.49 mbsf, and values finally returning to 0.4 ppm/wt% at the very top of the core. Mo was also plotted against TOC and the trend of these data correlate well with the Mo plots, especially the peaks in the upper half of the core (Figure 17) (Table 6, appendix).

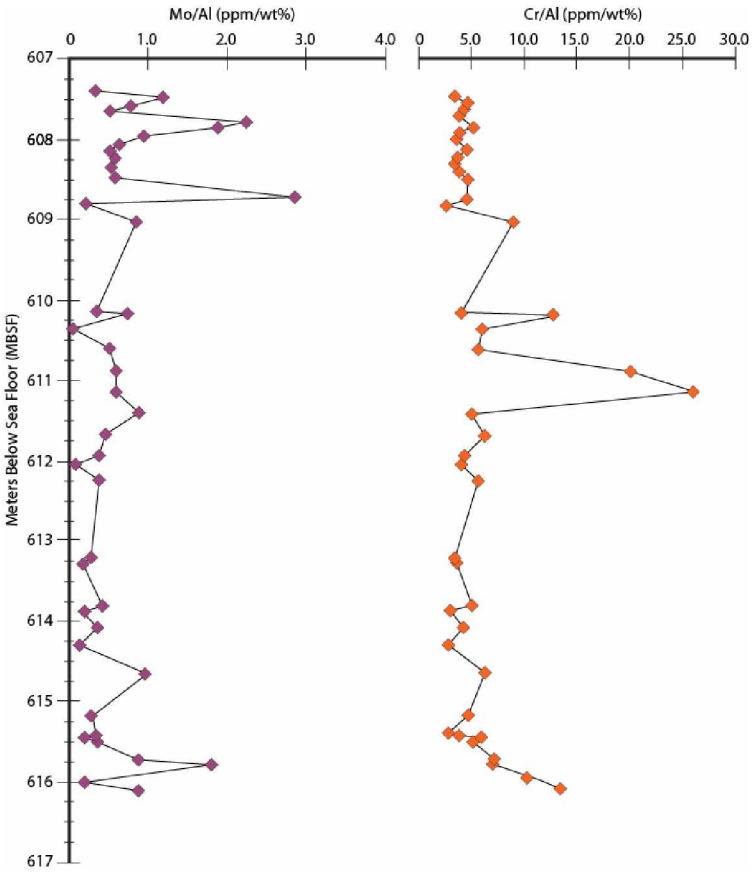

Figure 15, Redox Proxy Results

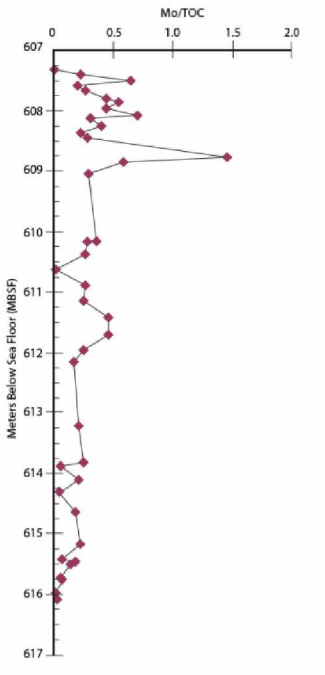

Figure 16, Mo/TOC

4.3.2 Productivity Proxies

Productivity Proxies are summarized in Table A-2 (appendix) and Figure 18.

Barium: The average Al normalized value of Ba in the studied section is 0.002 (wt%/wt%, unitless), and values range from 0.006 – 0.01. The base of the core begins with a high of 0.01, the highest value seen in the section. Values then drop significantly and ultimately go below the lower limit of detection (LLD) at 615.77 mbsf. Immediately following this, values show a slight rebound to 0.003 at 615.71 mbsf, then return to values closer to 0.002. These low values remain steady until 610.14 mbsf, where an increase to 0.003 is observed. From this point to the top of the core, values show a steady increase with the exception of two low values between 607.85 – 607.79 mbsf (0.001, 0.0009). Values then peak to the second highest in the section at 607.58 mbsf (0.007), and show significant elevation in the remaining two samples.

Zinc: The average Al normalized value of Zn in the studied section is 13.7 ppm/wt%, and values range from 8.2 – 48.6 ppm/wt%. The base of the core begins with a value of 24.0 ppm/wt% at 616.08 mbsf, which is immediately followed by a large peak of 48 ppm/wt% at 615.97. Values immediately come back down to 17 ppm/wt%, and remain stable (8-17 ppm/wt%) with little fluctuation throughout the rest of the core. At the very top, two stepwise increasing peaks occur at 607.79 with a value of 15.7 ppm/wt% and 607.58 with a value of 19.6 ppm/wt%.

Nickel: The average Al normalized value of Ni in the studied section is 4.6 ppm/wt%, with values ranging from 2.5 – 12.8 ppm/wt%. From the base of the core to 614.30 mbsf, there is a stepwise but clear declining trend that starts at 12.8 ppm/wt% and ultimately decreases to 3.8 ppm/wt% over the course of four decreasing magnitude peaks. From 614.3 – 610.14 mbsf Ni values are stable ranging from 2-4 ppm/wt%. The upper portion (609.02 – 608.74 mbsf) shows a positive trend, with values increasing from 4.3 – 6.3 ppm/wt%. Following this to the top of the core, values remain around the average, with two small pulses at 608.07 mbsf (4.7 ppm/wt%) and 607.65 mbsf (5.6 ppm/wt%).

Copper: The average Al normalized value of Cu in the studied section is 4.4 ppm/wt%, with values ranging from 1.5 – 16.5 ppm/wt%. With the exception of two data points, Cu proceeds in a similar, if not exaggerated fashion to Ni. The base is characterized by a two-step decline from 616.08 to 615.40 mbsf with values starting at 8.5 and decreasing to 4.1 ppm/wt%. However, the next two data points (615.16, 614.64 mbsf) show an increase to 8.6 and 16.5 ppm/wt%, respectively. The rest of the section mirrors Ni and Zn, albeit with larger fluctuations. From 614.3 – 610.14 mbsf there is a relatively stable section, with fluctuations from 1-6 ppm/wt%. This stable section is capped with a positive trend from 609.02 – 608.74 mbsf with values increasing from 4.8 – 6.2 ppm/wt%. Above this is another relatively stable section with the

average value slightly lower than the rest of the section (3.0 vs 4.4 ppm/wt%). The studied section is capped with a small peak of 6.0 ppm/wt% at 607.4 mbsf.

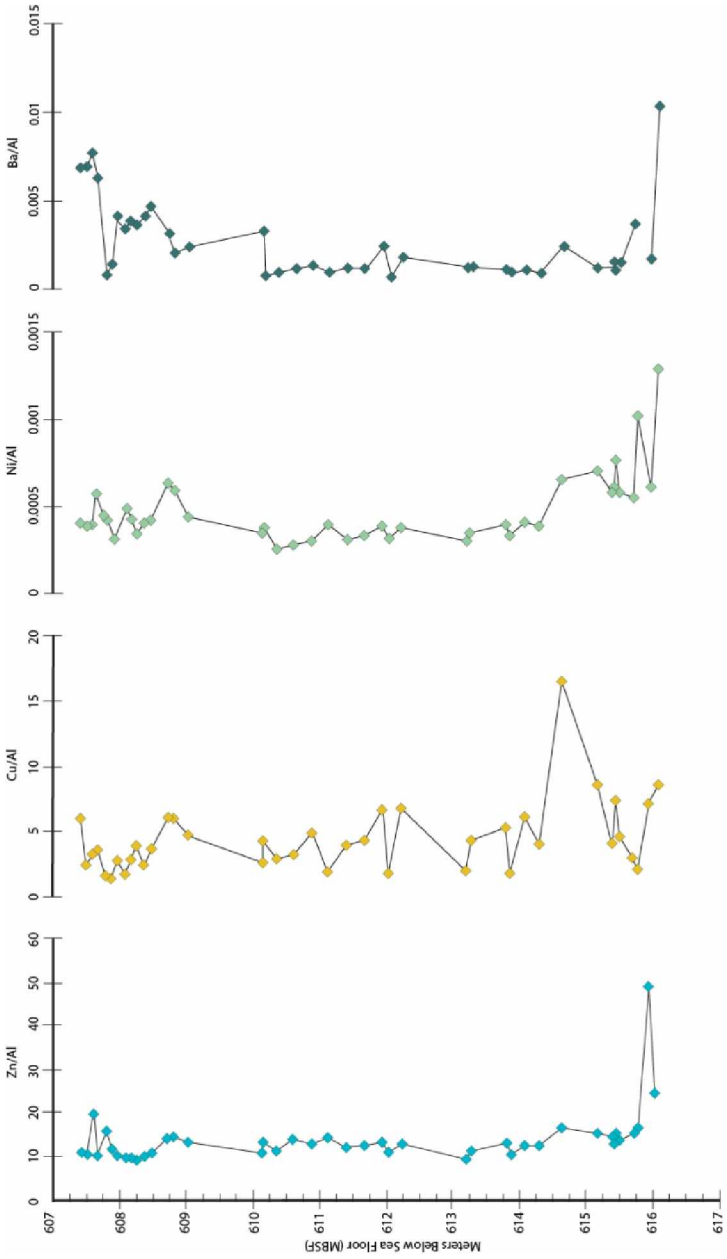

Figure 17, Productivity Proxy Results

4.3.3 Detrital Input Proxies

Detrital input proxies are summarized in Table A-3 (appendix) and Figure 19.

Silica: The average Al normalized value of Si in the studied section is 6.1 (wt%/wt%, unitless), with values ranging from 4.4 – 15.3. The base of the core begins with higher than average Si values (616.08 – 615.71 mbsf, 6.3 – 7.2). Overlying these values is a sharp decreasing trend from 615.49 – 615.43 mbsf with Si values decreasing from 6.3 to 4.8. This is followed by a length of relatively stable values ranging from 5.1- 6.3 from 615.40 – 610.17. This interval can be broken down into two sections; the first ranging from 615.40-613.21 mbsf shows a general decreasing trend culminating at a low of 4.4. This is followed by an increasing trend from 613.21 – 610.17 mbsf. The upper portion from 610.17 mbsf and above contains two stepwise troughs punctuated by two peaks, the first of which is at 610.14 mbsf with 4.5 and the second trough at 608.81 mbsf with 4.4. The section then shows a slight increasing trend, which culminates with a peak of 15.3 at 607.49 mbsf.

Titanium: The average Al normalized value of Ti in the studied section is 0.04 (wt%/wt%, unitless), with values ranging from 0.03 - 0.05. Overall normalized Ti values are very low and fluctuate only slightly throughout this section.

Aluminum: The average value of Al in the studied section is 2.5, and values range from 0.5 – 8.1. The base of the core starts off with an increasing trend from 616.08 – 615.43 mbsf. Values start at 0.5 wt% and peak at 3.6 wt% in this section. Following this is a gradual increasing then decreasing trend spanning 615.4 – 610.17 mbsf. This increasing trend starts at 615.40 with 2.1 wt% and continues to 613.21 mbsf with 5.1 wt%. This is followed by a decreasing trend which continues to 610.17 mbsf with a value of 1.5 wt%. Finally, the section is topped by two peaks

and a sharp decrease. The peaks occur at 610.14 and 608.81 mbsf with Al values of 4.2 and 8.0 wt% respectively. This is followed by a decrease back down to 1.9 wt% at 608.74 mbsf.

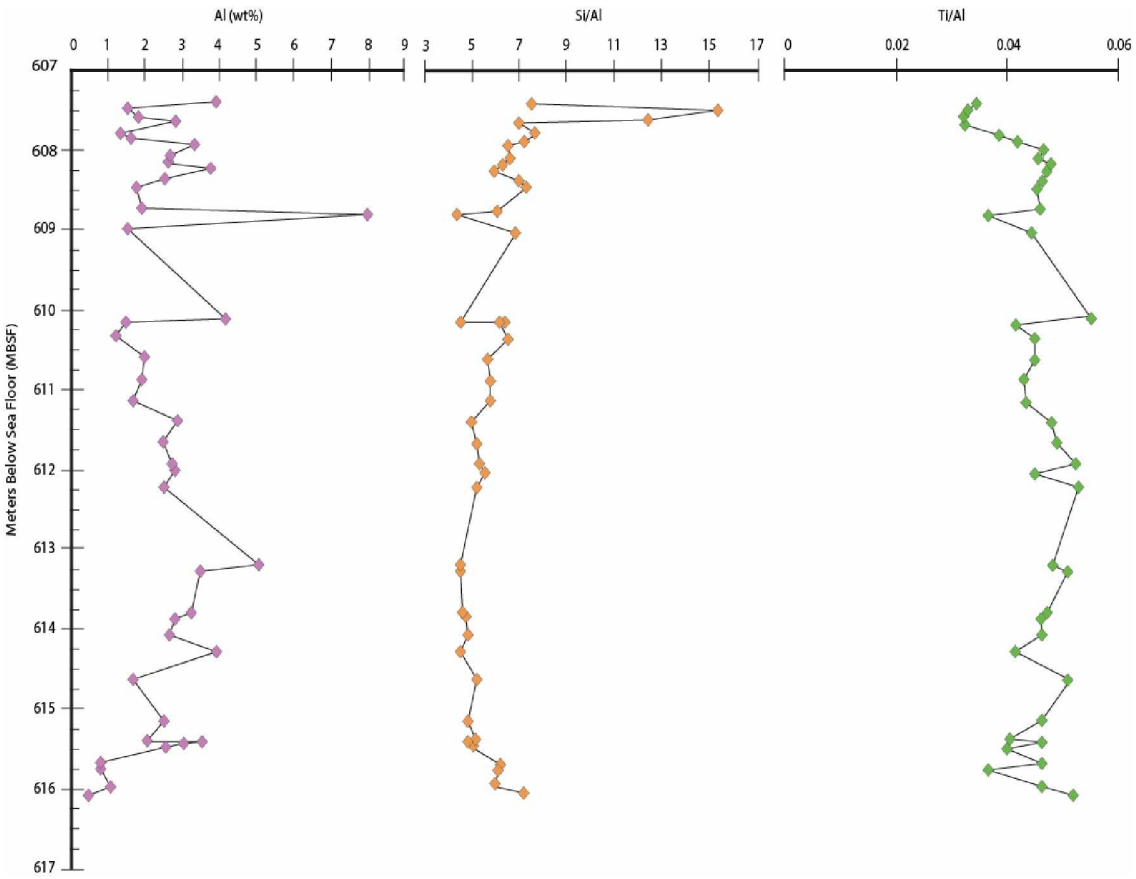

Figure 18, Detrital Input Proxy Results

4.4 Stable Isotopic Analyses: Carbon and Nitrogen

$\delta^{13}C_{org}$: The average value for $\delta^{13}C_{org}$ throughout the section is -26.8‰ and values range from -28.2‰ to -24.5‰. At the base of the section, $\delta^{13}C_{org}$ begins with a low value of -28.2‰ at 616.45 mbsf. From here, while fluctuation is observed, there is an overall increasing trend until 615.49 mbsf, culminating with a value of -26.52‰. From here until 610.61 mbsf, values change little, with only one slight negative excursion occurring at 613.87 mbsf. Above this is the one major positive excursion seen in the section at 610.36 mbsf with a $\delta^{13}C$ value of -24.5‰.

Immediately after, values return to pre-excursion levels, and the next perturbation is seen at 609.425 mbsf as a slight negative excursion to -27.78‰. Above this, in the uppermost portion of the core, values return to around the average with the data ending in an increasing trend and a final negative fluctuation down to -27.4‰ at 607.65 mbsf (Table A-4, Figure 20).

$\delta^{15}N_{bulk}$: The average value for $\delta^{15}N_{bulk}$ is 2.4‰, and values range from -2.1‰ to 4.4‰. At the base of the section, $\delta^{15}N_{bulk}$ begins with a value of 1.29‰. From there, an increasing trend is seen to 4.44‰ at 616.08 mbsf. Values then return to lower values at 615.77 mbsf (1.34‰). Another increase and decrease is seen immediately following this (615.71 – 615.44 mbsf, 3.14 – 1.06‰). Values then increase and seem to plateau around the core's average, and within this plateau are four negative $\delta^{15}N_{bulk}$ excursions. The first is at -613.87 mbsf, where it reaches a value of -1.55‰. The second negative excursion occurs shortly after at -613.21 and reaches a value of -1.26‰. The third negative excursion is at 610.89 MBSF and reaches a value of -2.06‰. The fourth and final negative excursion occurs at 609.385 and reaches a value of -1.86‰. Following this final negative excursion, values peak at 608.74 mbsf at 3.68‰, then show an overall decreasing trend with values going from 3.68 – 1.03‰ to the top of the core. These results are summarized in Table A-4, Figure 20.

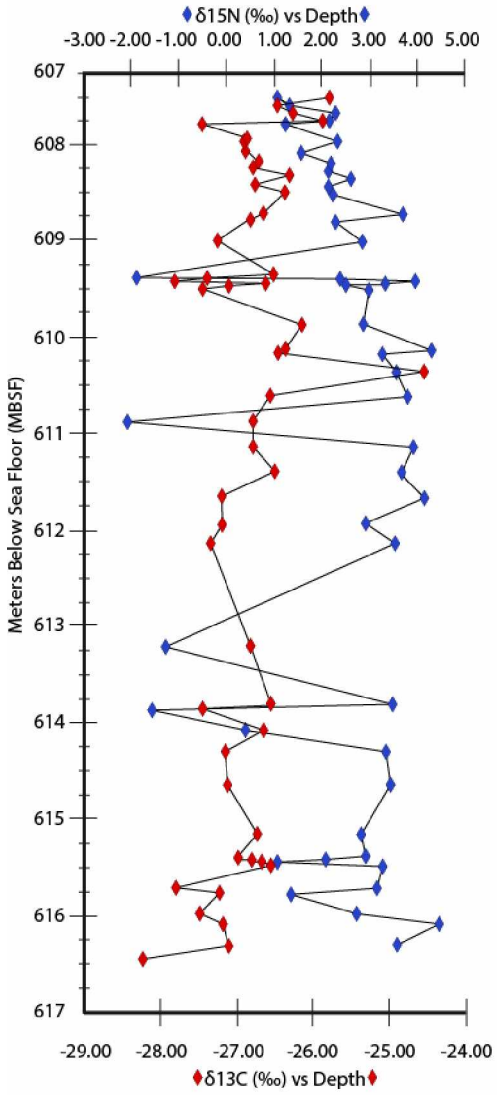

Figure 19, Stable Isotope Results

For both $\delta^{13}C_{org}$ and $\delta^{15}N_{bulk}$ a 13 cm section was sampled every centimeter. This section was chosen as it represents one full gradational claystone to foraminiferal wackestone cycle. The measured depth of this section ranges from 609.515 – 609.385 mbsf. $\delta^{13}C_{org}$ begins at 609.515 mbsf with a value of -27.2‰; values fluctuate around this number until 609.445, where they increase to -26.61‰. From there, a large decrease is seen to -27.78‰ at 609.425 mbsf. Following this, values increase to -26.51‰ at the top of this section. $\delta^{15}N_{bulk}$ values show much less change. From 609.515 – 609.395 mbsf, values stay consistently within 2 -4‰. However,

the uppermost point at 609.385 mbsf is a negative excursion of -1.86‰. In general, $\delta^{13}C_{org}$ and $\delta^{15}N_{bulk}$ covary until 609.445, where they then diverge and $\delta^{13}C_{org}$ increases and $\delta^{15}N_{bulk}$ decreases. These results are summarized in Figure 21.

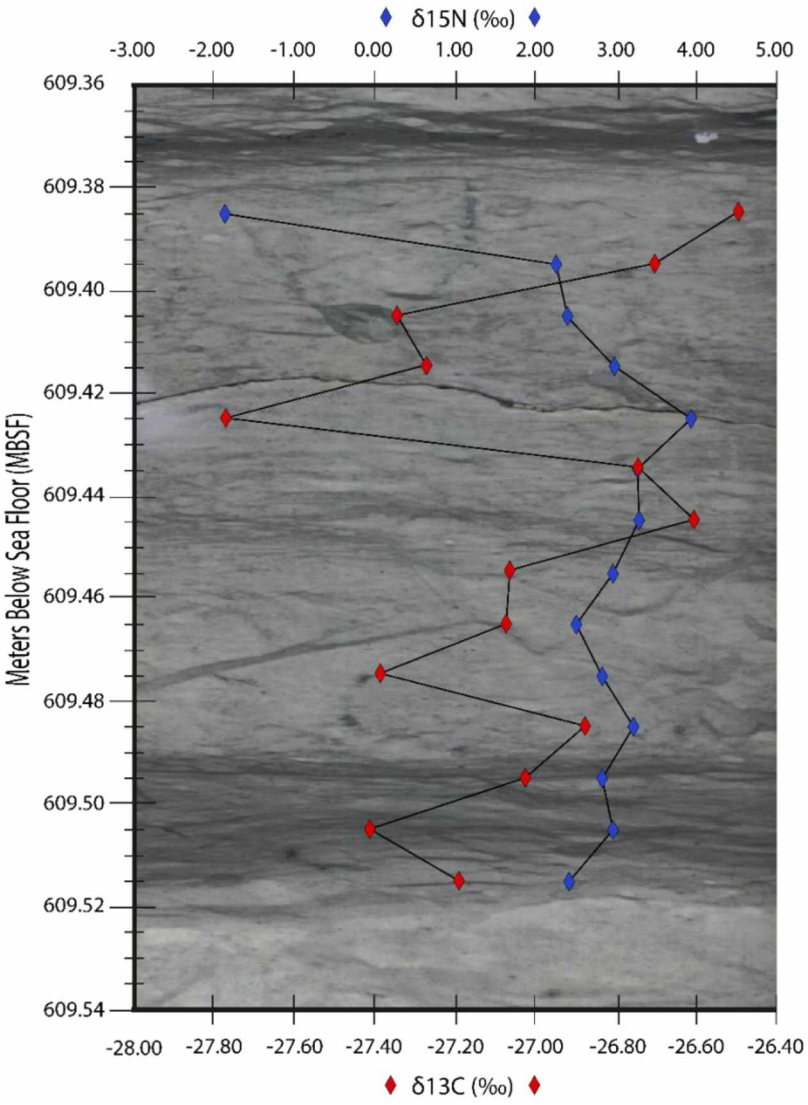

Figure 20, Stable Isotope Results from cm scale sampling

5. Discussion

At time of deposition, water depth was about 600 - 700m and located on the local high of the crater's peak ring (Lowery et al., 2018). The majority of facies seen are similar to typical

deep-water facies, with the primary rock type being bioturbated argillaceous wackestones to foraminiferal wackestones. Such fine-grained carbonates are the product of deposition in quiet, deep water settings (Flugel, 2004). In addition, the most prominent ichnotaxa seen within the core are *Zoophycos*, *Planolites*, and *Chondrites,* which are the dominant type until 607.74 mbsf. All of which occur in deeper continental margin settings (Rodriguez-Tovar et al., 2017).

The 72 identified cycles have been grouped into nine larger-scale packages and are interpreted as parasequences and systems tracts, respectively. These systems tracts can then be grouped into two complete and three partial depositional sequences, with complete sequences consisting of one full cycle of LST, TST, and HST. Throughout the core, several geochemical changes occur, and discussion of these geochemical changes will be in the framework of our identified sequences.

The identified sequences are as follows:

Sequence 1, 616.56 – 614.17 mbsf, complete sequence.

Sequence 2, 614.17 – 611.42 mbsf, incomplete TST, HST only sequence.

Sequence 3, 611.42 – 608.84 mbsf, complete sequence.

Sequence 4, 608.84 – 607.74 mbsf, incomplete sequence, contains only LST.

Sequence 5, 607.74 – 607.27 mbsf, incomplete sequence, contains only LST.

Several sequences are incomplete, most notably 4 and 5, which only contain lowstand systems tracts. The boundary between these however is a known unconformity, and the upper contact of sequence 5 is also a known unconformity. The contact between sequences 1 and 2 is

highly bioturbated and contains abundant pyrite, potentially signifying a non-depositional surface.

Due to the fact that any sedimentary record is affected by regional tectonics and local factors, our record alone cannot be interpreted in terms of eustatic sea level change. In order to put our data in a global context, published sequence stratigraphy from the Paleocene in New Jersey (Kominz et al., 2008) was used as a reference for our own interpretations as it is a well-studied region with demonstrated eustatic sea level change. Biostratigrapic zones from M0077 (Gulick et al., 2017) have allowed us to estimate the general duration of each sequence, systems tract, and parasequence.

5.1 Sequence 1

L-1, 616.56 – 616.04 mbsf, 66 – 65.5 my.

Lowstand 1 is the first systems tract identified in the Paleocene and begins at the Pα biostratigraphic boundary which is dated at 66 my. The boundary between biostratigraphic zones Pα and P1a occurs at 616.175 mbsf and is dated at 65.72 my, which lies within lowstand one. Using our estimation technique, we can place the upper boundary of lowstand one at 65.5 my. Comparing this to global sea level curves from Kominz (2008), Van Sickel et al. (2004), and Miller (2005), our observations are in line with a lowstand followed by an eustatic rise in sea level. This event in particular occurs prior to Miller (2005) and Kominz (2008) Pa1 eustatic highstand, meaning that this lowstand was global. In addition, this tract was deposited immediately following the K/Pg, when global sea levels were relatively low compared to the rest of the Cretaceous. New accommodation space had recently been created in the form of the crater itself, so our interpretation of a LST in the aftermath of the K/Pg event is in line with published

data. A rough estimate of sedimentation rates based on the location of the P1b biostratigraphic boundary and the thickness of lowstand 1 and transgression 1 puts both systems tracts at a rate of .17 cm/kyr.

Productivity proxies start out elevated in the Paleocene, and Ni has the highest value seen in the core, indicating increased productivity at this time. Detrital input and Mo are all low, and Cr shows a slight enrichment of 13. While it is often difficult to disentangle small enrichments of Cr from provincial sources, detrital input from Al in this section is near zero, suggesting that this enrichment is unrelated to sediment flux. Chromium has a much shorter residence time than Molybdenum (7-40kyr vs 800kyr) so it is possible that this initial elevated value is the result of a short variation in oxygenation. However, at this depth we see a coeval increase of $\delta^{15}N_{bulk}$, to its highest value in the studied section, likely the result of water column denitrification. While the Cr peak is a small enrichment, this is likely due to increased stagnation and reduced circulation that commonly occurs during lowstands.

$\delta^{13}C_{org}$ values at the base of the section (616.45 mbsf) are the lowest recovered from the core, which is understandable as this is the closest sample to the base of the Paleocene and the K/Pg extinction event (Hsü and MacKenzie, 1985). $\delta^{15}N_{bulk}$ values start relatively low and increase to about average, likely the result of increased fixation as productivity is at a local high.

These observations are in line with other published works using data from this core. Lowery et. al (in review), using microfossils and redox proxies, corroborates our interpretation of high productivity and increasing stagnation at this time. These interpretations are generally in line with what we know about the Gulf of Mexico in the early Danian. Not only do these results directly contradict the hypotheses that export productivity was shut off during this time

(D'Hondt et al., 1998) or that there was a complete shutdown of surface productivity (Hsu et al., 1985). They agree with other findings that show export productivity experienced an increase in the years post impact (Hull et al., 2011; Lowery et al., 2018).

T-1, 616.04 – 615.06 mbsf

The upper biostratigraphic boundary between P1a and P1b lies within the upper portion of this package (615.23 mbsf, 65.2 my). Since this biostratigraphic boundary is in close proximity to our identified stratigraphic boundary between T-1 and the overlying H-1 (17 cm from top), we can roughly estimate the termination of T-1 to be at about 65.1 my, making T-1 span from 65.5 – 65.1 my. Using this data we can make a rough estimate of sedimentation rates. The location of the P1b biostratigraphic boundary and the thickness of transgression 1 gives us a rate of .18 cm/kyr. Comparing this to global sea levels, transgression one is in line with eustatic sea level changes, and was deposited in a period of low to rising sea levels post K/Pg. This correlates with data from Kominz (2008), Van Sickel (2004), and Miller (2005).

Within this systems tract several major geochemical changes occur. At the base of the interval, productivity proxies indicate an environment with high productivity and redox proxies imply well oxygenated waters. Productivity is still generally at the highest it will be throughout the Paleocene, with peaks seen in Zn and Ni. However, variations among the proxies themselves exist. Copper, Barium, Zinc, and Nickel all start out elevated and show a decrease towards the top of this systems tract. Zinc begins at a lower value and then peaks a bit higher in the interval with Ni still displaying elevated levels. Mo is below its crustal average (1-2), and Cr shows a value just below the crustal average of 10. The elevations in productivity and low redox values suggest that the water was not only well oxygenated, pending seasonal fluxes we cannot detect at

this resolution, but also well mixed. Like L-1, this interpretation of high productivity in the early Danian is in line with previous work stating productivity increased in the Gulf post impact (Lowery et al., 2018). Prior studies have shown, however, that this increase was not seen across all oceans, and several locations saw a decline and slow recovery rates (Alegret et al., 2012). If distance from Chicxulub was the driving factor on timing of recovery, it would be expected that the crater itself recovered last. Yet here and in other publications we see a rapid increase in productivity post impact that is not seen in locations farther afield. This heterogeneity combined with our results further supports the importance of ecological factors and perhaps even random chance in the global recovery post K/Pg (Hull et al., 2011).

Directly overlying this interval of high productivity and oxygenated waters is an abrupt change that occurs from 615.97 – 615.71 mbsf. Immediately following the initial productivity boom, a sharp decline occurs among all productivity proxies except Ni. This is coincident with lower detrital input values and low Cr values. However, at this time both Mo and TOC (Figure 17) are elevated. While Mo values are not high enough to suggest anything beyond the potential for sulfidic pore waters, the high TOC is indicative of increased burial and preservation in lower oxygen environments. These changes are all congruent with the Dan C2 hyperthermal event, as the Dan C2 is associated with a period of low productivity and decreased detrital input (Lowery et al., in review). The Dan C2 event is also characterized by a double negative carbon isotope excursion (Quillevere et al., 2008), which is seen in our data in this interval (Figure 20). This is coupled with a small decrease in $\delta^{15}N_{bulk}$ values. The Dan C2 hyperthermal was likely the result of a short term, but rapid warming which caused an increase in stratification and a subsequent decrease in productivity (Lowery et al., in review) The Dan C2 event is also identified in Lowery et. al (in press) at this exact depth, supporting our interpretation.

Post Dan C2 event (615.71– 615.40 mbsf), Cr and Mo are below crustal average values, suggesting a well oxygenated environment. Cu and Ni show a rebound, while Zn remains low. This is perhaps caused by an increase in terrestrial flux, as aluminum peaks at this point. However, it is likely that export and primary productivity are still recovering from the Dan C2. An increase in carbon isotopes occurs post negative excursion, indicating productivity recovering (Figure 20).

H-1, 615.06 – 614.17 mbsf

This highstand is located entirely within biostratigraphic zone P1b, which occurs from 615.23 to 612.38 mbsf and is dated from 65.25 to 63.9 my. We would estimate that H-1 extends from 65.1 my at its base to roughly 64.5 my at the top. Given the 89 cm thickness, the sedimentation rate for this package is roughly 0.21 cm/kyr. This HST occurs during a period of rising global sea level (Kominz et al., 2008) and correlates to a highstand identified in the early Paleocene by Van Sickel et al. (2004).

The geochemical data in package two shows relatively stable values. Redox proxies remain consistently low, suggesting a prolonged period of well oxygenated waters. Zn and Ni both plateau, while Cu experiences a sharp peak that is coeval with a small peak in Zn (16.5-Cu; 17.8-Zn, 614.64 mbsf). This is the last increase in the overall decreasing productivity trend across all proxies from the base of the core to 614.64 mbsf. Calcispheres disappear and small foraminifera become more abundant, while large foraminifera make their first significant appearances. Both $\delta^{15}N_{bulk}$ and $\delta^{13}C_{org}$ are stable during this time. Once again, our interpretations are in line with other studies of M0077. Lowery et. al (2019) described a similar decrease in productivity at this time period, and linked it to an increase in spinose foraminifera,

citing that their wider diet was more suited towards lower nutrient waters. This is in line with our observation of increased foraminifera, and while detailed taxonomic identification was not part of this study, the foraminifera seen here do show an increase in spinose varieties.

5.2 Sequence 2

T-2 614.17 – 613.03 mbsf

With T-2 occurring entirely within biostratigraphic zone P1b, which falls between 615.23 to 612.38 mbsf and is dated from 65.25 to 63.9 my, a best estimate would place transgression 2 at 64.5 – 64.1 my with a sedimentation rate of 0.21 cm/kyr. This does not correlate with any published data. At this time, eustatic curves indicate sea level remaining in lowstand, suggesting this event is local. The base of T-2 is also highly bioturbated with an i.i. of 5. Due to this heavy bioturbation and abundant pyrite nodules, the contact between sequence 1 and 2 is being interpreted as a non-depositional surface.

Beginning at the base of this systems tract and immediately following the end of the productivity decline, all proxies enter a period of great stability. While Cu does fluctuate, these variations never deviate too far from the mean, and both Zn and Ni remain nearly static. This decrease in productivity is likely the result of the ocean regaining stratification once more. Export and primary productivity proxies are low through this section, indicating that the water column is no longer well mixed. One pulse of increased Al is seen (613.21 mbsf) which is associated with a coeval negative $\delta^{15}N_{bulk}$ excursion. As this is not associated with any other proxy change, it is possible that $\delta^{15}N_{bulk}$ values are influenced by clay minerals rather than organics.

H-2, 613.03 – 611.42 mbsf

With H-2 occurring entirely within the P1c biozone (612.38 mbsf, 63.9 my), with the P2 boundary above (610.63 mbsf, 63 my), a best estimate would place H-2 at 64.1 – 63.4 my with a sedimentation rate of 0.19 cm/kyr. Like T-2, this does not correlate with any published data, suggesting that this event is local. Similar to T-2, all proxies and isotopic data show little change with regard to their respective averages. This is interpreted as the continuation of a period of stability and ocean stratification. Again, this interpretation is in line with other published data, as Lowery et. al (in review) also identify this time as one of stability and stratification.

5.3 Sequence 3

L-2, 611.42 – 609.64 mbsf

With the P2 biostratigraphic boundary occurring within this systems tract (610.63 mbsf, 63 my) and the P3a boundary occurring above it (609.29 mbsf, 62.6 my), a best estimate places L-2 at 63.4 – 62.7 mya, resulting in a sedimentation rate of 0.25 cm/kyr. L-2 can be correlated with the lowstand prior to Miller et al. (2005) Pa1 and Kominz et al. (2008) PaG, suggesting that this LST was a eustatic event.

Within this package, a large peak in Cr occurs (25.5, 611.14 mbsf). This is the largest recovered value (Figure 16), exceeding the crustal average by a factor of two. Values are elevated beyond the average until 610.61 mbsf. This event is interpreted to be a period of anoxia. One negative nitrogen excursion occurs in this section at 610.89 mbsf. This value is not coincident with any other changes in isotopic data and is not correlated with TOC or changes in detrital input, so it is unlikely to be associated with increases in clay. However, it occurs when

Cr is still elevated above the average (19.7, 610.89 mbsf) which suggests that this negative $\delta^{15}N_{bulk}$ excursion is the product of an increase in fixation during a period of hypoxia. This occurred during a period of well-established ocean stratification (Lowery et al., in review) in the lead up to the Latest Danian Event (Juhle et al., 2015). This stratification could have been the driver for hypoxia.

$\delta^{13}C_{org}$ isotopes are relatively stable in the basal portion of this section, but a large positive excursion occurs towards the top at 610.36 mbsf. This is not concurrent with a major change in nitrogen data, but it occurs when Mo and Cr are at some of their lowest points and productivity and detrital input proxy values are low. This is also coeval with a massive increase in Ca and a general increase in TOC. This is likely due to an increase in preservation of organic matter during this time.

H-3, 609.64 – 608.84 mbsf

With the P3a biostratigraphic boundary occurring within H-3 (609.29 mbsf, 62.6 my), and P4b occurring above it (607.65 mbsf, 57.79 my), a best estimate places H-3 at 62.7 – 61.1 my with a sedimentation rate of roughly .05 cm/kyr. This can be correlated to the Miller et al. (2005) (Pa1) and Kominz et al. (2008) (PaF) global highstands.

Within this package we were able to sample a full cycle for $\delta^{13}C_{org}$ and $\delta^{15}N_{bulk}$ values (609.385 – 609.515 mbsf). Stable isotope data taken at the centimeter scale show an overall increase in $\delta^{13}C_{org}$ values from base to top, and relatively stable $\delta^{15}N_{bulk}$ values until a sharp decrease at the uppermost centimeters, which contain the final negative $\delta^{15}N_{bulk}$ excursion (-1.9, 609.385 mbsf). The presence of these values at the top of a cycle where the proportion of skeletal grains and the i.i. is much higher than the base is not surprising. The increase in $\delta^{13}C_{org}$

and decrease in $\delta^{15}N_{bulk}$ both suggest increasing productivity, which is supported by the i.i. and and skeletal grain proportion. While interesting to note, the pattern for this cycle cannot be applied to all cycles across the core. Several samples taken from the tops of cycles have revealed high $\delta^{15}N_{bulk}$ values and one of the negative excursions was taken from a cycle base. It is important to note however, that in the absence of multiple proxy data points throughout this or any other single cycle, it would be difficult to interpret whether or not this trend reflected the norm in our section.

However, within this centimeter scale $\delta^{13}C_{org}$ and $\delta^{15}N_{bulk}$ sampling, data show covariation between $\delta^{13}C_{org}$ and $\delta^{15}N_{bulk}$ values until 609.445 mbsf where they diverge (Figure 21).

Within this centimeter-scale sampling, we see the second lowest $\delta^{13}C_{org}$ value of the entire Paleocene (-27.78‰ at 604.425 mbsf). This is coeval with a slight increase in $\delta^{15}N_{bulk}$ values to 3.95 ‰. This excursion is of particular interest due to its location at the base of H-3. Using our time estimation technique, this event can be dated to roughly about 62.3 my. Given that our technique is a rough estimate, it is within reason that our negative $\delta^{13}C_{org}$ excursion is the Latest Danian Event (LDE) which was dated to 62.18 my (Jehle et al., 2015). In addition, a decrease in small and large foraminifera is seen as well as increases in lime mud and pyrite through this specific interval (Table A-1). The LDE was characterized by a warming of the entire water column, and disappearance of many benthic foraminifera (Jehle et al., 2015), which the results of this study support.

Beyond the centimeter-scale sampling, neither $\delta^{13}C_{org}$ nor $\delta^{15}N_{bulk}$ show much deviation from their respective averages. Geochemical samples were not able to be taken from this section due to sample size constraints.

There is only one geochemical proxy sample from this tract, and all values show little deviation from their respective averages.

5.4 Sequence 4

Lowstand 3, 608.84 – 607.74 mbsf

A best estimate of age for L-3 given the location of the P3a and P4b biostratigraphic boundaries is 61.1 -57.7 my, with the upper boundary being directly below an unconformity and the P4b boundary, giving it a sedimentation rate of 0.03 cm/kyr. This can be correlated to the lowstand between the Miller et al. (2005) Pa1 and Pa2 highstands or the lowstand between the PaF and PaE highstands of Kominz et al. (2008). In addition, this correlates with published data from Liu et al., 2019, which studied third order sequences from the East China Shelf Basin. A 1.2 my periodicity was identified and compared with previous studies (Miller 2005, Kominz 2008) and found to be in general agreement, therefore the results of that study are believed to show obliquity as the driver of these sea level changes. Because our data here aligns with all three studies, we can infer that obliquity was the driver for this event as well. (Liu et al., 2019)

Within this package, detrital input has a sharp peak in Al (608.81 mbsf) which coincides with a decrease in all redox proxies and a small increase in all productivity proxies except Ba. This is immediately overlain by the largest Mo peak in the core (2.9, 608.74 mbsf), at which point productivity still remains slightly elevated and there is a slight positive increase in $\delta^{15}N_{bulk}$ to 3.7. While this Mo value is still low, it is above average and coupled with the increase in

denitrification, we can assume that this is the continuation of ocean stratification and the presence of a redox gradient. Following this, values across all proxies return to near their respective averages.

5.5 Sequence 5

Lowstand 4, 607.74 – 607.27 mbsf

At its base, package six is a claystone capped by an unconformity. The facies seen post unconformity are drastically different from the rest of the core; lithologies range from packstone to claystone to grainstone, rather than the usual wackestones of the lower portion of the Paleocene. The increase in species variety and presence of shallower water ichnofabrics coupled with the uppermost facies presenting as a hardground suggest a period of falling sea levels that was ultimately capped by the Paleocene – Eocene boundary. This tract correlates with published eustatic data, and can be traced to the time between Miller et al. (2005) Pa3 highstand or Kominz et al. (2008) PaC and PaB highstand. Like Sequence 4, Sequence 5 can also be correlated with Liu et al. (2019), suggesting that this event was also driven by obliquity.

This interpretation is supported by the geochemical data. Redox proxies are consistently low, and detrital input in Al and Si is higher than the average for the rest of the core. Si in particular has a large peak at 607.49 mbsf, as silicified clasts are common, but this is due to secondary remineralization. Ba reaches its highest value in the core (0.24, 607.58 mbsf). Coupled with the general trend of increasing $\delta^{13}C_{org}$, all data points towards a highly productive period, likely caused by increasing temperatures towards the end of the Paleocene.

6. Conclusions

Stratigraphic and geochemical analysis of M0077 provide valuable insight into the Paleocene at Chicxulub. 72 identified parasequences can be grouped into five larger stratigraphic sequences and with the exception of those in sequence 2 (64.5-63.4 my), all sea level changes are caused by eustatic change. These sequences experience changes in geochemistry indicating variations in their environment and several major events. The following conclusions can be drawn from our data:

In the initial million years post-impact, Chicxulub crater experienced a period of high to declining productivity. Comparing with other locations around the world, this was a relatively rapid recovery and supports the hypothesis that spatial variation in recovery timing was controlled by ecological factors as well as random chance. The random chance hypothesis is furthered by the fact that despite being ground zero for the impact, Chicxulub experienced much quicker recovery than some locations that were significantly farther away.

Following this period of high productivity was a period of declining to low productivity that lasted for the duration of the Paleocene. While this period was the result of the crater returning to more "normal" conditions, several events did punctuate the Paleocene. The Dan-C2 event (65.2 my) is characterized by a sharp decrease in productivity and a negative $\delta^{13}C_{org}$ excursion, both of which can be seen in the core. The second event that punctuated the Paleocene was a hypoxic event at 611.14 mbsf (roughly 63 my). This event occurred in a lowstand and is thought to be the result of increased stratification during this time. The final event seen in the core is a negative $\delta^{13}C_{org}$ excursion occurring at 609.42 mbsf (61.6 my), which is assumed to be the Latest Danian Event. The uppermost Paleocene is characterized by an increase in $\delta^{13}C_{org}$ and high

export productivity values, and is punctuated by two unconformities, with the core ending in the PETM.

Literature Cited

Alegret, L., E. Thomas, and K.C. Lohmann (2012), End-Cretaceous marine mass extinction not caused by productivity collapse, Proceedings of the National Academy of Sciences, 109(3), 728-732.

Algeo, T.J., Lyons, T.W., 2006.Mo-total organic carbon covariation in modern anoxic marine environments: implications for analysis of paleoredox and paleohydrographic conditions. Paleoceanography 21.

Alvarez, L.W., Alvarez, W., Asaro, F., Michel, H.V., 1980. Extraterrestrial cause of the Cretaceous–Tertiary extinction. Science 208, 1095–1108.

Artemieva N. et al., 2017, Quantifying the Release of Climate-Active Gases by Large Meteorite Impacts With a Case Study of Chicxulub, *Geophysical Research Letters*, ISSN: 0094-8276

Catuneanu, O., Abreu, V., Bhattacharya, J.P., *et al*, Towards the standardization of sequence stratigraphy, Earth-Science Reviews, Volume 92, Issues 1–2, 2009, Pages 1-33, ISSN 0012-8252, https://doi.org/10.1016/j.earscirev.2008.10.003.

Cole, D.B., Zhang, S., Planavsky, N., A new estimate of detrital redox-sensitive metal concentrations and variability in fluxes to marine sediments, Geochimica et Cosmochimica Acta, Volume 215, 2017, Pages 337-353, ISSN 0016-7037, https://doi.org/10.1016/j.gca.2017.08.004.

Collins, G., Morgan, J., Barton, P., *et al*, Dynamic modeling suggests terrace zone asymmetry in the Chicxulub crater is caused by target heterogeneity, Earth and Planetary Science Letters,Volume 270, Issues 3–4, 2008, Pages 221-230

De Oca C, Martinez-Ruiz F, Rodriguez-Tovar FJ (2013) Bottom-Water Conditions in a Marine Basin after the Cretaceous–Paleogene Impact Event: Timing the Recovery of Oxygen Levels and Productivity. PLoS ONE 8(12): e82242. doi:10.1371/journal.pone.0082242

Droser, M.L., and Bottjer, D.J., 1986, A semiquantitative field classification of ichnofabric: Journal of Sedimentary Petrology, v. 56, p. 558–559

Dunham, R.J., 1962, Classification of carbonate rocks according to depositional texture, in Hamm, W.E., ed., Classification of carbonate rocks—A Symposium: AAPG Mem. v. 1, p. 108–121.

Embry, A.F., III, and Klovan, J.E., 1972, Absolute water depths of late Devonian paleoecological zones: Geologische Rundschau, v, 61, p. 672–686.

Esmeray-Senlet, S., Wright, J.D., Olsson, R.K., Miller, K.G., Browning, J.V., and Quan, T.M. (2015). Evidence for reduced export productivity following the Cretaceous/Paleogene mass extinction, Paleoceanography, 30, doi:10.1002/2014PA002724.

Flugel E., (2004), Microfacies of Carbonate Rocks: Analysis Interpretation, and Application: Springer Verlag.

Gulick, S., Barton, P., Christeson, G. *et al.* Importance of pre-impact crustal structure for the asymmetry of the Chicxulub impact crater. *Nature Geosci* **1,** 131–135 (2008). https://doi.org/10.1038/ngeo103

Gulick, S., Morgan, J., Mellett, C.L., and the Expedition 364 Scientists, 2017. *Expedition 364 Preliminary Report: Chicxulub: Drilling the K-Pg Impact Crater.* International Ocean Discovery Program. http://dx.doi.org/10.14379/iodp.pr.364.2017

Gulick, S., Morgan, J., Mellett, C.L., and the Expedition 364 Scientists, 2017. *Site M0077: Post Impact Sedimentary Rocks.* International Ocean Discovery Program. https://doi.org/10.14379/iodp.proc.364.105.2017

Hildebrand, A.R., Penfield, G.T., Kring, D.A., Pilkington, M., Camargo, A.Z., Jacobsen, S.B., Boynton, W.V., 1991. Chicxulub Crater: a possible Cretaceous/Tertiary boundary impact crater on the Yucatán Peninsula, Mexico. Geology 19, 867–871.

Hollis, C.J. , Strong, C.P. , Rodgers, K.A. & Rogers, K.M. (2003). Paleoenvironmental changes across the Cretaceous/Tertiary boundary at Flaxbourne River and Woodside Creek, eastern Marlborough, New Zealand, New Zealand

Hsü, K.J., & McKenzie, J.A. (1985). A "Strangelove" ocean in the earliest Tertiary. *The Carbon Cycle and Atmospheric CO: Natural Variations Archean to Present*, 487-492.

Hull, P. M. Norris, R.D., Bralower, T. J. & Schueth, J.D. A role for chance in marine recovery from the end-Cretaceous extinction. *Nat. Geosci.* **4**, 856–860 (2011).

Jablonski, D. (1995) in *Extinction Rates* (eds. Lawton, J. H. & May, R. M.) 25–44 Oxford Univ. Press, Oxford.

Kominz, M.A., Browning, J.V., Miller, K.G., Sugarman, P.J., Mizintseva, S. and Scotese, C.R. (2008), Late Cretaceous to Miocene sea-level estimates from the New Jersey and Delaware coastal plain coreholes: an error analysis. Basin Research, 20: 211-226. doi:10.1111/j.1365-2117.2008.00354.x

Kring, D. A. (2007). The Chicxulub impact event and its environmental consequences at the Cretaceous–Tertiary boundary: *Palaeogeography, Palaeoclimatology, Palaeoecology*, 255, 4-21.

Li, L., Keller, G., Variability in Late Cretaceous climate and deep waters: evidence from stable isotopes, Marine Geology, Volume 161, Issues 2–4, 1999, Pages 171-190, ISSN 0025-3227, https://doi.org/10.1016/S0025-3227(99)00078-X.

Liu, Y., Huang, C., Ogg, J.G., Algeo, T., Kemp, D.B., Shen, W., Oscillations of global sea-level elevation during the Paleogene correspond to 1.2-Myr amplitude modulation of orbital obliquity cycles, Earth and Planetary Science Letters, Volume 522, 2019, Pages 65-78, ISSN 0012-821X, https://doi.org/10.1016/j.epsl.2019.06.023

Lowery, C.M. and Fraass, A.J. (2018). Explanation for delayed recovery of species diversity following the end Cretaceous mass extinction. *PaleoRxiv Preprint:* https://paleorxiv.org/wn8g6

Lowery, C, Bralower, T., Owens, J., *et al*, (2018). Rapid Recovery of Life at Ground Zero of the End Cretaceous Mass Extinction. Nature. 558. 10.1038/s41586-018-0163-6.

Lowery, C., Jones, H., Bralower, T., *et al*, (in review). Early Paleocene Paleoceanography and Export Productivity in the Chicxulub Crater. 10.31223/osf.io/j8fsd.

MacLeod, K. G., Quinton, P. C., Sepúlveda, J., & Negra, M. H. (2018). Postimpact earliest Paleogene warming shown by fish debris oxygen isotopes (El Kef, Tunisia). *Science*, *360*(6396), 1467–1469. https://doi.org/10.1126/science.aap8525

Miller, K.G., Kominz, M.A., Browning, J.V., Wright, J.D., Mountain, G.S., Katz, M.E., Sugarman, P.J., Cramer, B.S., Christie-Blick, N. & Pekar, S.F. (2005) The Phanerozoic record of global sea-level change. Science, 310,1293-1298.

Morgan JV, 2016, The formation of peak rings in large impact craters, *Science*, Vol:354, ISSN:0036-8075, Pages:878-882

Morgan, J.V., S.P.S. Gulick, C.L. Mellet, S.L. Green, and Expedition 364 Scientists (2017) *Chicxulub: Drilling the K-Pg Impact Crater, Proceedings of the International Ocean Discovery Program, 364*, International Ocean Discovery Program, College Station, TX doi: 10.14379/iodp.proc.364.103.2017.

Pope, K., Baines, K., Ocampo, A., Ivanov, B., Impact winter and the Cretaceous/Tertiary extinctions: Results of a Chicxulub asteroid impact model, Earth and Planetary Science Letters, Volume 128, Issues 3–4, 1994, Pages 719-725, ISSN 0012-821X, https://doi.org/10.1016/0012-821X(94)90186-4.

Quillévéré, F., Norris, R.D., Kroon, D., and Wilson, P.A. (2008). Transient ocean warming and shifts in carbon reservoirs during the early Danian. *Earth and Planetary Science Letters*, 265, 600-615.

Rodriguez-Tovar, F. J., Whalen, M. and OMalley, K., Morgan, J., Guilick, S., Mellett, C. L., and Expedition 364 Scientists, (2017), Zoophycos Through Paleocene Sediments from the IODP-ICDP Expedition 364: Paleoenvironmental Changes After the Chicxulub Impact, Lunar and Planetary Science XLVIII

Schulte, P. and 40 others, (2010), The Chicxulub asteroid impact and mass extinction at the Cretaceous-Paleogene boundary, Science, 327, 1214-1218.

Scott, C., Lyons, T., (2012), Contrasting molybdenum cycling and isotopic properties in euxinic versus non-euxinic sediments and sedimentary rocks: Refining the paleoproxies. Chemical Geology. s 324–325. 19–27. 10.1016/j.chemgeo.2012.05.012.

Śliwiński, M. G., Whalen, M. T., Newberry, R. J., Payne, J. H., and Day, J. E., 2011, Stable isotope (δ13Ccarb and org, δ15Norg) and trace element anomalies during the Late Devonian 'punctata Event' in the Western Canada Sedimentary Basin: Palaeogeography, Palaeoclimatology, Palaeoecology, v. 307, no. 1-4, p. 245-271.

Tribovillard N., Thomas A., Timothy L., Armelle R. 2015. Trace Minerals as Paleoredox and Paleoproductivity Proxies: An Update. Chemical Geology. vol. 232 no. 1-2, pp. 12-32.

Van Sickel, W.A., Kominz, M.A, Miller, K.G. & Browning, J.V. (2004) Late cretaceous and cenozoic sea-level estimates backstripping analysis of borehole data, Onshore New Jersey. Basin Res., 16, 451-465.

Van Wagoner, J.C., Posamentier, H. W., Mitchum, R. M., Vail, P. R., Sarg, J. F., Loutit, T. S., Hardenbol, J.,1988. "An Overview of the Fundamentals of Sequence Stratigraphy and Key Definitions", Sea-Level Changes: An Integrated Approach, Cheryl K. Wilgus, Bruce S. Hastings, Henry Posamentier, John Van Wagoner, Charles A. Ross, Christopher G. St. C. Kendall

Vellekoop, J., Sluijs, A., Smit, J., Schouten, S., Weijers, J.W.H., Sinninghe Damsté, J.S., Brinkhuis, H., 2014. Rapid short-term cooling following the Chicxulub impact at the Cretaceous–Paleogene boundary. PNAS 2014, 111, 7537-7541.

Vellekoop, J., Woelders, L., Açikalin, S., Smit, J., Van De Schootbrugge, B., Yilmaz, I.O., Brinkhuis, H., and Speijer, R. (2017). Ecological response to collapse of the biological pump following the mass extinction at the Cretaceous-Paleogene boundary. *Biogeosciences*, 14, 885-900.

Ward, W C., Keller, G., Stinnesbeck, W., Adatte, T., "Yucatan Subsurface Stratigraphy: Implications and Constraints for the Chicxulub Impact." *Geology*, 1995.

Whalen, M T., Gulick S., Pearson, Z., Norris R., Perez-Cruz, Urrutia-Fucugauchi, 2013. Annealing the Chicxulub Impact: Paleogene Yucatan Carbonate Slope Development in the Chixulub impact basin, Mexico. SEPM Special Publication 105

Zachos, J.C., Arthur, M.A., & Dean, W.E. (1989). Geochemical evidence for suppression of pelagic marine productivity at the Cretaceous/Tertiary boundary. *Nature*, 337, 61-64

Appendix: Data Tables and Large Figures

TABLE A-1, POINT COUNTING DATA

Depth (MBSF)	Small Foram	Large Foram	Lime Mud	Calcisphere	Algae	Brachiopod	Gastropod	Echinoderm	Unknown	Intraclast	Pyrite	Calcite Cement
607.31	41.90%	7.60%	30.00%	0.00%	8.00%	0.60%	0.00%	0.60%	1.60%	0.60%	0.60%	8.00%
607.79	26.30%	2.60%	67.00%	0.00%	0.00%	0.00%	0.00%	0.00%	0.00%	0.00%	1.00%	3.00%
608.24	27.30%	0.60%	66.00%	0.00%	0.00%	0.00%	0.00%	0.60%	0.00%	0.00%	1.00%	4.30%
608.74	41.30%	0.30%	48.30%	0.00%	0.00%	0.00%	0.00%	0.00%	0.30%	0.00%	7.30%	2.30%
609.32	33.00%	1.00%	54.00%	0.00%	0.00%	0.00%	0.00%	0.00%	0.00%	0.30%	4.60%	7.00%
609.59	45.00%	1.60%	41.00%	0.00%	0.00%	0.00%	0.00%	0.00%	0.00%	0.00%	1.60%	10.60%
610.17	31.30%	0.30%	50.30%	0.00%	0.00%	0.00%	0.00%	0.00%	2.00%	0.00%	2.00%	14.00%
610.61	27.60%	0.00%	55.60%	0.00%	0.00%	0.00%	0.00%	0.00%	0.00%	0.00%	3.30%	13.30%
611.14	28.30%	0.00%	57.60%	0.00%	0.00%	0.00%	0.00%	0.00%	0.00%	0.00%	0.30%	13.60%
611.94	48.00%	0.00%	33.00%	0.00%	0.00%	0.00%	0.00%	0.00%	0.00%	0.00%	0.00%	18.90%
613.21	35.60%	0.00%	47.00%	0.00%	0.00%	0.00%	0.00%	0.00%	0.00%	0.00%	0.00%	17.30%
613.8	43.00%	1.00%	44.60%	0.00%	0.00%	0.00%	0.00%	0.00%	0.00%	0.00%	0.30%	11.00%
614.3	39.00%	1.00%	48.30%	0.00%	0.00%	0.00%	0.00%	0.00%	2.00%	0.00%	0.30%	9.30%
614.9	30.30%	3.30%	58.00%	0.00%	0.00%	0.00%	0.00%	0.00%	0.00%	0.00%	0.30%	8.00%
615.43	15.60%	0.30%	64.30%	7.60%	0.00%	0.00%	0.00%	0.00%	0.30%	0.30%	0.00%	11.30%
615.71	13.30%	0.00%	64.60%	18.30%	0.00%	0.00%	0.00%	0.00%	0.00%	0.00%	0.00%	3.60%
616.08	6.00%	0.30%	72.60%	16.60%	0.00%	0.00%	0.00%	0.00%	0.00%	0.00%	0.00%	4.30%

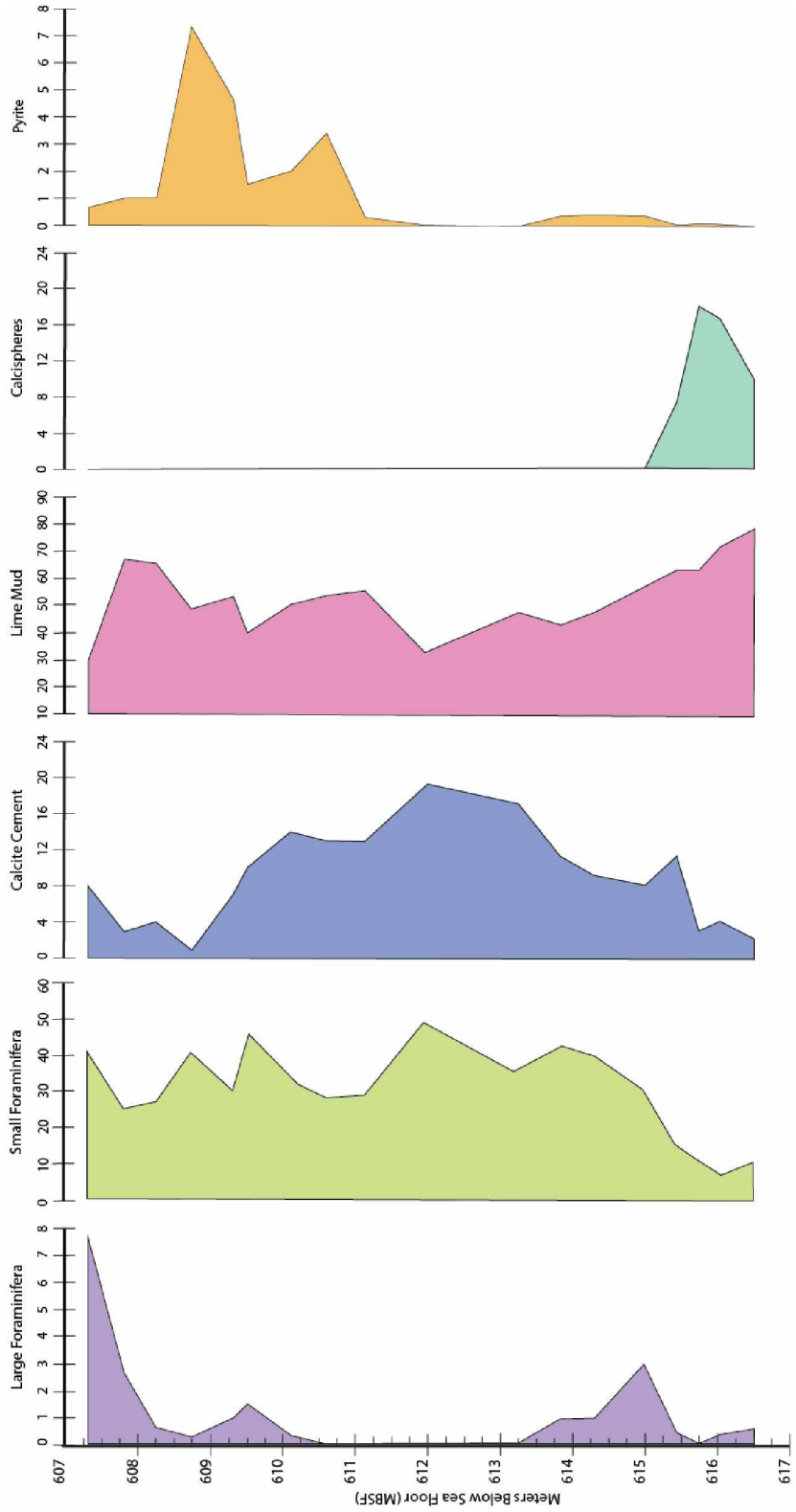

FIGURE A-1, POINT COUNTING DATA

TABLE A-2 PRODUCTIVITY AND REDOX PROXIES

Depth (mbsf)	V	Cr	Ni	Cu	Zn	Mo
607.40	3.603	3.317	3.919	6.001	10.730	0.298
607.49	1.424	4.744	3.808	2.542	10.419	1.166
607.58	2.249	4.157	3.850	3.401	19.632	0.752
607.65	2.424	3.860	5.656	3.630	10.104	0.491
607.79	1.938	5.237	4.090	1.678	15.740	2.224
607.85	4.347	3.939	4.010	1.529	11.655	1.853
607.95	5.493	3.589	2.918	2.840	10.045	0.911
608.07	6.409	4.542	4.797	1.882	9.621	0.605
608.15	5.213	3.677	4.109	3.009	9.850	0.491
608.24	5.580	3.332	3.365	3.985	9.137	0.551
608.35	5.076	3.852	3.924	2.553	9.689	0.510
608.45	4.560	4.661	4.163	3.796	10.681	0.559
608.74	6.319	4.107	6.352	6.206	14.158	2.868
608.81	6.840	2.250	5.914	6.009	14.950	0.196
609.02	5.309	8.494	4.328	4.827	13.275	0.844
610.14	5.830	3.702	3.502	2.566	10.158	0.328
610.17	3.966	12.684	3.550	4.515	12.671	0.733
610.36	4.118	5.629	2.557	2.949	10.478	0.037
610.61	6.222	5.300	2.757	3.263	14.053	0.506
610.89	6.085	19.716	3.002	4.878	12.609	0.594
611.14	6.180	25.592	3.968	1.940	14.506	0.588
611.41	6.664	4.675	3.058	3.981	11.624	0.883
611.67	7.089	6.030	3.393	4.474	12.128	0.462
611.94	6.284	3.955	3.842	6.735	13.359	0.374
612.04	4.064	3.820	3.199	1.810	10.032	0.056
612.23	6.175	5.229	3.748	6.780	12.653	0.374
613.21	4.920	2.878	2.946	2.028	8.242	0.262
613.28	5.742	3.135	3.476	4.272	10.837	0.165
613.80	5.410	4.612	3.903	5.239	12.914	0.408
613.87	3.431	2.739	3.286	1.762	9.433	0.195
614.08	4.033	3.772	4.097	6.197	12.095	0.346
614.30	3.808	2.311	3.848	4.063	12.090	0.119
614.64	4.252	5.822	6.541	16.508	17.850	0.967
615.16	3.991	4.303	7.081	8.635	15.859	0.288
615.40	2.797	2.437	5.819	4.155	14.828	0.326
615.43	3.056	3.392	6.124	4.350	13.041	0.180
615.44	3.954	5.496	7.626	7.411	15.936	0.331
615.49	2.591	4.708	5.802	4.648	13.655	0.362
615.71	0.000	6.734	5.490	3.011	15.890	0.868
615.77	0.000	6.600	10.197	2.126	17.464	1.808
615.97	3.038	10.234	6.021	7.110	48.644	0.168
616.08	0.000	13.009	12.833	8.598	24.066	0.867

TABLE A-3, DETRITAL INPUT AND BARIUM

Depth (mbsf)	Al	Si	Ti	Ba
607.40	3.994	7.536	0.035	0.0069
607.49	1.597	15.352	0.033	0.0069
607.58	1.881	12.496	0.032	0.0078
607.65	2.877	7.030	0.032	0.0062
607.79	1.344	7.599	0.039	0.0009
607.85	1.666	7.212	0.042	0.0014
607.95	3.410	6.499	0.046	0.0041
608.07	2.738	6.617	0.045	0.0034
608.15	2.673	6.316	0.048	0.0039
608.24	3.839	5.955	0.047	0.0037
608.35	2.586	6.981	0.046	0.0041
608.45	1.833	7.360	0.046	0.0046
608.74	1.974	6.092	0.046	0.0032
608.81	8.052	4.410	0.037	0.0019
609.02	1.627	6.847	0.044	0.0025
610.14	4.259	4.533	0.055	0.0033
610.17	1.559	6.384	0.042	0.0006
610.36	1.299	6.538	0.045	0.0009
610.61	2.081	5.661	0.045	0.0013
610.89	2.027	5.805	0.043	0.0014
611.14	1.783	5.759	0.043	0.0011
611.41	2.919	5.031	0.048	0.0013
611.67	2.533	5.177	0.049	0.0012
611.94	2.876	5.333	0.052	0.0025
612.04	2.861	5.509	0.045	0.0008
612.23	2.632	5.217	0.053	0.0018
613.21	5.133	4.452	0.049	0.0012
613.28	3.583	4.505	0.051	0.0013
613.8	3.282	4.679	0.047	0.0011
613.87	2.899	4.788	0.046	0.0009
614.08	2.696	4.827	0.046	0.0011
614.30	3.953	4.549	0.042	0.0009
614.64	1.743	5.228	0.051	0.0023
615.16	2.584	4.832	0.046	0.0012
615.40	2.192	5.120	0.040	0.0013
615.43	3.621	4.837	0.041	0.0010
615.44	3.128	4.934	0.046	0.0016
615.49	2.629	5.055	0.040	0.0015
615.71	0.922	6.295	0.047	0.0037
615.77	0.900	6.176	0.037	-
615.97	1.419	5.909	0.041	0.0010

TABLE A-4, CN DATA

Depth (mbsf)	d15N	d13C
607.31	1.037	-25.777
607.40	1.24	-26.459
607.49	2.246	-26.259
607.58	2.095	-25.866
607.65	1.171	-27.458
607.79	2.188	-26.852
607.85	2.244	-26.891
607.95	1.485	-26.885
608.07	2.121	-26.679
608.15	2.036	-26.766
608.24	2.539	-26.31
608.35	2.07	-26.739
608.45	2.156	-26.354
608.74	3.68	-26.63
608.81	2.30	-26.79
609.02	2.86	-27.21
609.32	2.174	-26.708
609.385	-1.86	-26.51
609.395	2.24	-26.71
609.405	2.39	-27.35
609.415	2.98	-27.28
609.425	3.95	-27.78
609.435	3.28	-26.76
609.445	3.29	-26.61
609.455	2.99	-27.07
609.465	2.53	-27.08
609.475	2.84	-27.40
609.485	3.24	-26.98
609.495	2.85	-27.03
609.505	2.98	-27.42
609.515	2.41	-27.20
609.58	2.535	-26.594
609.88	2.86	-26.12
610.14	4.29	-26.34
610.17	3.27	-26.43
610.36	3.57	-24.53
610.61	3.81	-26.54
610.89	-2.06	-26.77
611.14	3.92	-26.76
611.41	3.67	-26.48
611.67	4.13	-27.16
611.94	2.94	-27.16
612.14	3.54	-27.33
612.85	2.815	-27.042
613.21	-1.26	-26.80
613.8	3.47	-26.53
613.87	-1.55	-27.42
614.08	0.41	-26.63
614.30	3.34	-27.13
614.64	3.44	-27.10
615.16	2.81	-26.70
615.40	2.94	-26.96
615.43	2.07	-26.78
615.44	1.06	-26.65
615.49	3.25	-26.52
615.71	3.14	-27.75
615.77	1.34	-27.20
615.97	2.71	-27.46
616.08	4.44	-27.17
616.305	3.58	-27.09

TABLE A-5, MO/TOC DATA

Depth	TOC	Mo/TOC
607.40	1.269	0.235
607.49	1.798	0.652
607.58	3.414	0.220
607.65	1.792	0.274
607.79	5.106	0.436
607.85	3.353	0.553
607.95	2.023	0.451
608.07	0.853	0.710
608.15	1.617	0.304
608.24	1.370	0.402
608.35	2.228	0.229
608.45	1.869	0.299
608.74	1.963	1.461
608.81	0.331	0.593
609.02	2.828	0.298
610.14	0.910	0.361
610.17	2.576	0.285
610.36	2.651	0.277
610.61	2.238	0.017
610.89	1.909	0.265
611.14	2.334	0.255
611.41	1.278	0.460
611.67	1.915	0.461
611.94	1.824	0.253
612.14	2.160	0.173
613.21	1.190	0.220
613.8	1.622	0.252
613.87	3.050	0.064
614.08	1.607	0.216
614.3	2.298	0.052
614.64	5.034	0.192
615.16	1.301	0.221
615.40	3.740	0.087
615.43	2.327	0.077
615.44	1.704	0.194
615.49	2.297	0.158
615.71	13.726	0.063
615.77	24.487	0.074
615.97	15.466	0.011
616.08	28.081	0.031